Fakultät für Physik
Institut für Theorie der Kondensierten Materie

Another thesis on SNS junctions: numerical simulations and calculations

Master's Thesis

by

Umut Nefta Kanilmaz

Submission date: 25. February 2018

Advisor: PD Dr. Igor Gornyi
Co-Advisor: Prof. Dr. Alexander Mirlin

Ich erkläre hiermit, dass die Arbeit selbstständig angefertigt, alle benutzten Quellen und Hilfsmittel vollständig und genau angegeben und alles kenntlich gemacht wurde, das aus Arbeiten anderer unverändert oder mit Abänderungen entnommen ist.

Karlsruhe, den 23. Februar 2018

Umut Nefta Kanilmaz

Contents

1 Introduction

Lorem ipsum dolor sit amet, consetetur sadipscing elitr, sed diam nonumy eirmod tempor invidunt ut labore et dolore magna aliquyam erat, sed diam voluptua. At vero eos et accusam et justo duo dolores et ea rebum. Stet clita kasd gubergren, no sea takimata sanctus est Lorem ipsum dolor sit amet. Lorem ipsum dolor sit amet, consetetur sadipscing elitr, sed diam nonumy eirmod tempor invidunt ut labore et dolore magna aliquyam erat, sed diam voluptua. At vero eos et accusam et justo duo dolores et ea rebum. Stet clita kasd gubergren, no sea takimata sanctus est Lorem ipsum dolor sit amet.

2 Experimental set-up

2.1 First: summary of paper

2.1.1 Introduction

Josephson effect [1] has been studied a lot. Key challenge: Developing devices in which the induced superconductivity can be monitored. This experiment is cool, because it uses local gates to control confinement, amplitude and density profile of the supercurrent. The sample used is a BLG-HBN-VDW heterostructure. Tunnel barrier -¿ supercurrent can only be tuned by modifying the geometry/temperature. Weak link -¿ a conductive material, in which superconductivity can be induced (proximity effect) and supercurrent can flow over larger distance than in tunnel junction [2]. Magnitude of supercurrent depends on contact transparency, disorder in the weak link, temperature.

Greatness of this work: full control of supercurrent both in amplitude and spatial distribution has not been observed so far. It is difficult to confine charge carriers in graphene (SLG!), because no backscattering in graphene and Klein tunneling [3]. Using BLG helps, because one can engineer an electronic band gap forming the barrier.

Sample geometry: QPC-like split gate geometry. The sample is overall gated with a backgate V_{BG}, a local top-gate in shape of two fingers (QPC geometry) is used to build a barrier. How does this process work? The overall backgate pushes the fermi level up into the conductance band. The topgate gives a displacement field, it pushes the fermi level down into the band gap −¿ no conduction possible, insulating state induced. Asymmetry between the layers of bilyer graphene (different energies at the layer) opens a band gap [4] that is tuneable.

Normal state analysis:

- low charge carrier density $2.8 \cdot 10^{18}$.

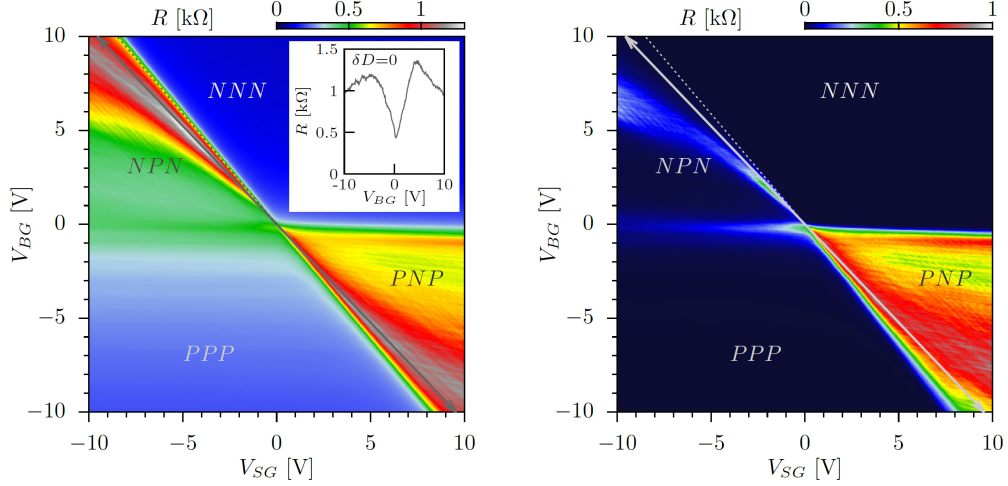- Landau fans in magnetotransport measurement

- Fabry Perot interferences
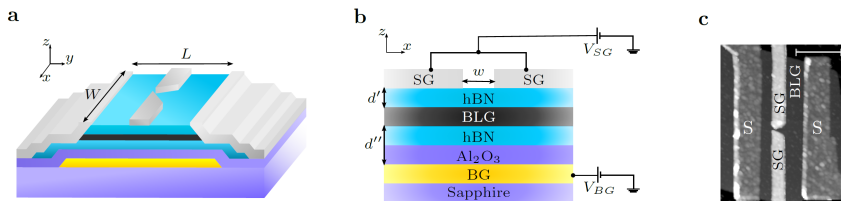
Figure 2.1: *Resistance maps*

On the resistance maps

The gate map has the backgate as y-axis, the splitgate (QPC topgate) as x-axis and the color indicates the strength of measured resistane. For orientiation, the line where back and splitgate are equal is called the displacement field line (grey arrow). Naming the regions, depending on the position of the fermi level: fermi level in valence band: N, fermi level in conductance band: P. Think of it as three regions: BLG backgated, the area where BLG is back and topgated (region with topgates on top of the material), and again a region where BLG is only backgated. Depending on the the choice of V_{BG} and V_{SG}, there are four regions: NNN, NPN, PPP, PNP. Looking at the upper left quadrant, NPN. In this region, the maximum resistance seems to follow the displacement field line (grey arrow), until a certain point, where it bends and the maximum resistance is not on a straight line anymore. Effect is visible in the normal state but even more in the superconducting state. −¿ unexpected behaviour.

Explanation? Charge carrier density is low, the influence of the backgate is important. The higher the backgate value is, the less the charge carrier density is affected by the splitgate and the stray fields, that it produces. And, as the splitgate impact is weak, the device stays conductive (resistance is low) along the displacement field line. Why the bending? In the upper region of the displacement field line, the split gates work as intenden: the channel region (the region, where the supercurrent can pass through) is conductive, because the backgate dominates. In the region, where the resistance curve is bending, the stray fields from the splitgate dominate, effectively blocking the channel region and therefore leading to to increased resistance.

The overall resistance is higher on the p-side, due to the slight n-doping of the leads (they create a pn junction at each contact). Can be seen in the supercondcuting state, the pnp region remains resistive, the npn region shows zero resistance.

Fabry Perot resonances

gate dependece of conductance shows oscillatory behaviour, are attributed to Fabry Perot interferences of different cavities [5]

Superconducting state

Since the device becomes superconducting in the npn region, the experiments focus on this part when analysing the supercurrent.
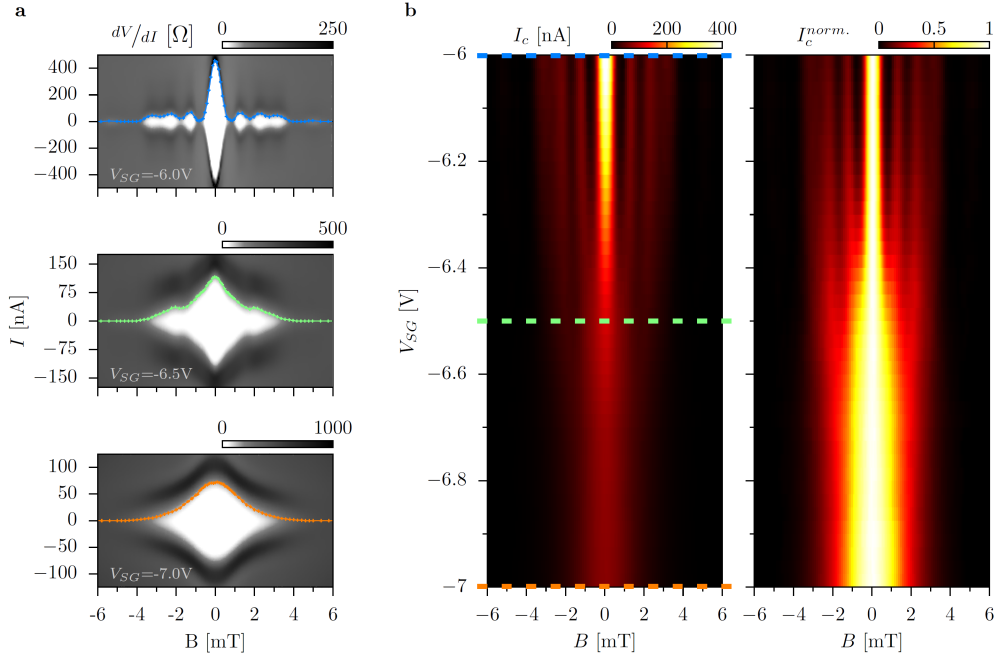
The amplitude of the supercurrent can be monitored by tuning the charge carrier densitiy with the backgate.

Supercurrent density can be explored by probing the interference pattern in response to a perpendicular magnetic field. A change of the junction geometry directly manifests within the interference pattern.

Confinement of the current can be observerd:

- open regime: Fraunhofer-like pattern, two dimensional system

- splitgate increases: lobes are lifted

- constriction is formed, really a 1D channel has formed: non beating, bell-shaped pattern

Transition from Fraunhofer to bell-shaped pattern has been observed before: [6]

3 **Framework for analytical model**

3.1 **Theory of superconductivity**

The discovery of the isotope effect in 1950 revealed that not only lattice electrons but rather the whole lattice determines the superconducting properties of a solid. Experiments measuring the critical temperature T_c of different mercury isotopes showed that, indeed, there is a relation between the isotope mass and T_c. Herbert Fröhlich was then the first to introduce a new concept to explain superconductivity. He showed that a phonon-mediated interaction between electrons and the lattice could lead to an attractive long-range interaction of electrons in the lattice. Figuratively speaking, an electron passing through the crystal lattice will polarize it by attracting the positive ions. It leaves a deformed lattice, which will then attract a second electron. An effective attractive interaction between these two electrons is thereby created. In 1956, Cooper showed that the electronic ground state, the Fermi sea at $T = 0$, is unstable if a weak attractive interaction is taken into account. This layed the foundation of the BCS theory [?], the first successful microscopic theory after the discovery of superconductivity in 1911 by Heike Kammerlingh Onnes.

Preliminaries

The BCS Hamiltonian reads

$$H = H_0 + H_1 \tag{3.1}$$

$$H_0 = \sum_{\mathbf{k},\sigma} \xi_{\mathbf{k}} c_{\mathbf{k}\sigma}^\dagger c_{\mathbf{k}\sigma} \tag{3.2}$$

$$H_1 = \frac{1}{N} \sum_{\mathbf{k},\mathbf{k}'} V_{\mathbf{k}\mathbf{k}'} c_{\mathbf{k}\uparrow}^\dagger c_{-\mathbf{k}\downarrow}^\dagger c_{-\mathbf{k}'\downarrow} c_{\mathbf{k}'\uparrow} \tag{3.3}$$

The operators $c_{\mathbf{k},\sigma}^\dagger$ and $c_{\mathbf{k},\sigma}$ are fermion operators that create or annihilate an electron with momentum $\mathbf{k}$ and spin σ. The first term in the Hamiltonian H is the unperturbed electron Hamiltonian H_0 with parabolic energy dispersion $\xi_{\mathbf{k}}$. The second term is the interaction Hamiltonian H_1, expressing the scattering of two electrons from $(\mathbf{k}' \downarrow, -\mathbf{k}' \uparrow)$ to $(\mathbf{k} \uparrow, -\mathbf{k} \downarrow)$. The interaction potential $V_{\mathbf{k},\mathbf{k}'}$ exchanges the scattering for electrons with energy $|\xi_{\mathbf{k}}| \lesssim \hbar\omega_D$.

The Hamiltonian in eq. (3.1) can be simplified by a mean-field approximation. In this approximation, an operator A is expressed by a sum of its statistical mean $\langle A | A \rangle$ and small statistical fluctuations δA. Since the fluctuations are assumed to be small, terms with $\mathcal{O}((\delta A)^2)$ can be

neglected.

$$A = \langle A \rangle + \delta A, \quad B = \langle B \rangle + \delta B$$
$$AB = \langle A \rangle \langle B \rangle + \langle A \rangle \delta B + \langle B \rangle \delta A + \underbrace{\delta A \delta B}_{\approx 0} \tag{3.4}$$

Using $\delta A = A - \langle A \rangle$ and inserting this back into eq. (3.4) leads to

$$AB = \langle A \rangle B + \langle B \rangle A - \langle A \rangle \langle B \rangle. \tag{3.5}$$

This approximation is applied to the interaction part H_1 in eq. (3.3), replacing

$$A = c_{\mathbf{k}\uparrow}^{\dagger} c_{-\mathbf{k}\downarrow}^{\dagger}, \quad B = c_{-\mathbf{k}'\downarrow} c_{\mathbf{k}'\uparrow}. \tag{3.6}$$

The result is the BCS-Hamiltonian

$$H_{\mathrm{BCS}} = \sum_{\mathbf{k},\sigma} \xi_{\mathbf{k}} c_{\mathbf{k}\sigma}^{\dagger} c_{\mathbf{k}\sigma} - \sum_{\mathbf{k}} \Delta_{\mathbf{k}}^{*} c_{-\mathbf{k}\downarrow} c_{\mathbf{k}\uparrow} - \sum_{\mathbf{k}} \Delta_{\mathbf{k}} c_{\mathbf{k}\uparrow}^{\dagger} c_{-\mathbf{k}\downarrow}^{\dagger} + \mathrm{const.} \tag{3.7}$$

where

$$\Delta_{\mathbf{k}} := -\frac{1}{N} \sum_{\mathbf{k}'} V_{\mathbf{k}\mathbf{k}'} \langle c_{-\mathbf{k}'\downarrow} c_{\mathbf{k}'\uparrow} \rangle \tag{3.8}$$

$$\Delta_{\mathbf{k}}^{*} := -\frac{1}{N} \sum_{\mathbf{k}'} V_{\mathbf{k}\mathbf{k}'} \langle c_{\mathbf{k}'\uparrow}^{\dagger} c_{-\mathbf{k}'\downarrow}^{\dagger} \rangle \tag{3.9}$$

The BCS-Hamiltonian in eq. (3.7) can be diagonalized using the Bogoliubov transformation. The aim is to express the Hamiltonian in the basis of new fermion operators. These new operators will describe quasiparticles, which are a linear combination of $c_{\mathbf{k},\sigma}^{\dagger}$ and $c_{\mathbf{k},\sigma}$.

$$\begin{pmatrix} \gamma_{\mathbf{k}\uparrow} \\ \gamma_{-\mathbf{k}\downarrow}^{\dagger} \end{pmatrix} = \begin{pmatrix} u_{\mathbf{k}}^{*} & -v_{\mathbf{k}} \\ v_{\mathbf{k}}^{*} & u_{\mathbf{k}} \end{pmatrix} \begin{pmatrix} c_{\mathbf{k}\uparrow} \\ c_{-\mathbf{k}\downarrow}^{\dagger} \end{pmatrix} \tag{3.10}$$

Evaluating the fermion anticommutation relation using the transformation above yields

$$\left\{ \gamma_{\mathbf{k}\uparrow}, \gamma_{\mathbf{k}\uparrow}^{\dagger} \right\} = \cdots = |u_{\mathbf{k}}|^2 + |v_{\mathbf{k}}|^2 \overset{!}{=} 1 \tag{3.11}$$

and will lead to the inverse transformation of eq. (3.1). Inserting the inverse transformation into the BCS-Hamiltonian in eq. (3.7) will give the coefficients $u_{\mathbf{k}}$, $v_{\mathbf{k}}$ from eq. (3.1) and finally yield to the diagonalized form of the BCS-Hamiltonian

$$H_{\mathrm{BCS}} = \sum_{\mathbf{k}\sigma} E_{\mathbf{k}} \gamma_{\mathbf{k}\sigma}^{\dagger} \gamma_{\mathbf{k}\sigma} \tag{3.12}$$

$$E_{\mathbf{k}} := \sqrt{\xi_{\mathbf{k}}^2 + |\Delta_{\mathbf{k}}|^2} \tag{3.13}$$

For a fixed energy $E_k \overset{!}{=} \epsilon$, eq. (3.13) gives two possible values for ξ_k:

$$\xi_{\mathbf{k}} = \pm\sqrt{\epsilon^2 - |\Delta_{\mathbf{k}}|^2}. \tag{3.14}$$

Knowing that $k^2 = k_F^2 \pm 2m\sqrt{\epsilon^2 + |\Delta_k|^2}\hbar^2$, one can calculate the group velocity as

$$v_g = \frac{d\epsilon}{d(\hbar k)} = \pm v_F \frac{\sqrt{\epsilon^2 - |\Delta|^2}}{\epsilon}. \tag{3.15}$$

The group velocity is positive for excitations outside the Fermi surface and negative for excitations inside. Therefore, the positive solution is a particle-like excitation, and the negative solution is a hole-like excitation. Figure 3.1 shows the excitation spectrum of particles and holes from the BCS theory.
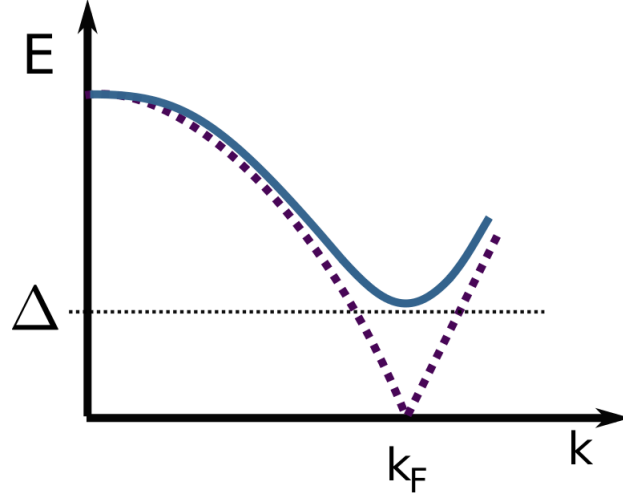
Figure 3.1: *Excitations from BCS theory. The dashed line is the normal state dispersion relation ($\Delta = 0$). The solid line is the dispersion relation for the superconducting state ($\Delta \neq 0$), where no excitations with energies $\epsilon < \Delta$ are present.*

Bogoliubov de Gennes Hamiltonian

The ansatz for the BCS ground state used by Bardeen, Cooper and Schrieffer is based on the concept of Cooper pairs. It is a direct consequence of the instability in the ground state through the attractive interaction. The BCS theory proposes a BCS ground state built on eigenstates of the single-particle Hamiltonian H_0 from eq. (3.2), leading to a ground state that consists of a linear combination of pair states.

$$|\psi_{\text{BCS}}\rangle = \prod_{\mathbf{k}} (u_{\mathbf{k}} + v_{\mathbf{k}} c_{\mathbf{k}\uparrow}^{\dagger} c_{-\mathbf{k}\downarrow}^{\dagger}) |\text{vac}\rangle \tag{3.16}$$

$$H_{\text{BCS}} |\psi_{\text{BCS}}\rangle = E_{\text{BCS}} |\psi_{\text{BCS}}\rangle \tag{3.17}$$

In most cases however, a more realistic set-up or inhomogeneous system cannot be described in terms of eigenfunctions of H_0. With a vector potential $\mathbf{A} \neq 0$, for example, time reversal symmetry is not given any more. The characteristic length scale is the superconducting coherence length ξ_0. If a system is varying slowly over a length scale $l \approx \xi_0$, a spatially dependent, more general Hamiltonian is needed. In order to find an adequate expression for such a spatially dependent Hamiltonian, the following spinor is introduced

$$|\Psi_{\mathbf{k}}\rangle = \begin{pmatrix} |\Psi_{\mathbf{k_1}}\rangle \\ |\Psi_{\mathbf{k_2}}\rangle \end{pmatrix} := \begin{pmatrix} c_{\mathbf{k},\uparrow}^{\dagger} \\ c_{-\mathbf{k},\downarrow} \end{pmatrix} |\psi_{\text{BCS}}\rangle \tag{3.18}$$

In this basis $\left\{ |\Psi_{\mathbf{k_1}}\rangle, |\Psi_{\mathbf{k_2}}\rangle \right\}$, the Hamiltonian (3.7) takes the form known as the Bogoliubov de Gennes Hamiltonian

$$H_{\text{BdG}}(\mathbf{k}) = \begin{pmatrix} \xi_{\mathbf{k}} & -\Delta_{\mathbf{k}} \\ -\Delta_{\mathbf{k}}^{*} & -\xi_{\mathbf{k}} \end{pmatrix}. \tag{3.19}$$

The energies are measured relative to $E_{\mathbf{k}}$ and a constant E_{BCS} has been neglected. This Hamiltonian form eq. (3.19) has the eigenvalues

$$\pm E_{\mathbf{k}} = \pm \sqrt{\xi_{\mathbf{k}}^2 + |\Delta_{\mathbf{k}}|^2}. \tag{3.20}$$
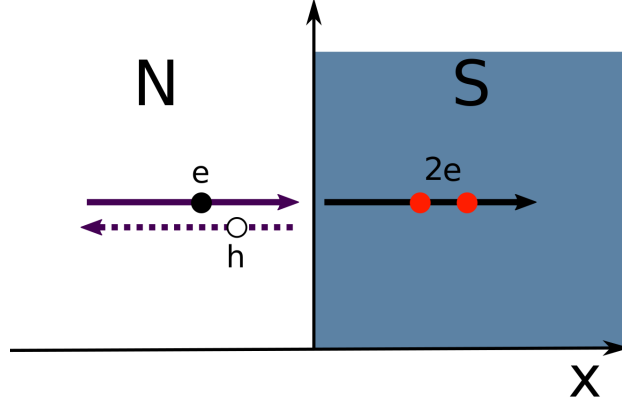
Figure 3.2: *Andreev reflection at an NS interface. An incoming electron is Andreev reflected into a hole with opposite momentum, and a Cooper pair condensates into the superconductor. The interface is modelled as a sharp edge.*

To finally arrive at the spatially dependent form of eq. (3.19), the Hamiltonian is Fourier-transformed.

$$H_{\text{BdG}}\left(\mathbf{r}\right) \quad := \quad \frac{1}{N}\sum_{\mathbf{k}}e^{i\mathbf{k}\cdot\mathbf{r}}H_{\text{BdG}}\left(\mathbf{k}\right) \tag{3.21}$$

$$= \quad \begin{pmatrix} H_0\left(\mathbf{r}\right) & -\Delta\left(\mathbf{r}\right) \\ -\Delta^*\left(\mathbf{r}\right) & -H_0\left(\mathbf{r}\right) \end{pmatrix} \tag{3.22}$$

$H_0\left(\mathbf{r}\right)$ is the free Hamiltonian. Corresponding Schrödinger equations are called BdG-equations:

$$H_{\text{BdG}}\left(\mathbf{r}\right)\Psi\left(\mathbf{r}\right) \quad = \quad E\Psi\left(\mathbf{r}\right) \tag{3.23}$$

$$\Psi\left(\mathbf{r}\right) \quad = \quad \begin{pmatrix} \Psi_1\left(\mathbf{r}\right) \\ \Psi_2\left(\mathbf{r}\right) \end{pmatrix}. \tag{3.24}$$

3.2 Andreev reflection at the interfaceb between a superconductor and a normal metal

Now that the principles of BCS theory have been established, the physical effects at the interface between a superconductor and a normal metal are to be outlined.

The most important detail when modelling the interface between a superconductor (S) and a normal metal (N) is the superconducting order parameter $\Delta\left(\mathbf{r}\right)$. It is present in the superconducting region and zero in a normal metal. To keep the model as simple as possible, a step-like behaviour is assumed. This means that for an interface placed at $x = 0$, the superconducting order parameter becomes a function of x and can be written as

$$\Delta\left(x\right) = \theta\left(x\right)\Delta_0. \tag{3.25}$$

How does the eigenvalue problem (3.23) with the potential (3.25) differ from a quantum mechanical step potential set-up? The formalism is virtually identical, but there is a subtle and important difference in the results. In the normal region, there are electrons, whereas in the superconducting regions, there is a condensate of Cooper pairs. A normal electron can be reflected at the interface as a hole and an additional Cooper pair can be created in the superconducting region (see figure

3.2). By solving the Bogoliubov-de-Gennes equation in (3.23), this picture becomes clearer. This equation needs to be solved both for the normal and the superconducting region. When treating this problem quantum-mechanically, energies below and above the gap need to be considered independently. The resulting wave functions have to be continuous at the interface. Depending on the region, the gap parameter in the Hamiltonian in eq. (3.22) is either zero or Δ_0.

Semi-classical approximation: Andreev equations

With the NS interface, the gap parameter varies slowly over scales of k_F^{-1}, and it may vary over scales of the coherence length ξ_0. Because k_F^{-1} is a good length scale for this problem, the equations above can be simplified:

$$\Psi\left(\mathbf{r}\right) = e^{i\mathbf{k_F r}} \begin{pmatrix} u\left(\mathbf{r}\right) \\ v\left(\mathbf{r}\right) \end{pmatrix}. \tag{3.26}$$

Since $u\left(\mathbf{r}\right)$ and $v\left(\mathbf{r}\right)$ vary slowly over distances of order k_F^{-1}, the second derivative with respect to $\mathbf{r}$ can be neglected. This approach is called the semi-classical approximation, which allows to transform the BdG eqs. (3.23) into the Andreev equations

$$-i\hbar\mathbf{v}_F\nabla u\left(\mathbf{r}\right) + \Delta\left(\mathbf{r}\right)v\left(\mathbf{r}\right) = \epsilon u\left(\mathbf{r}\right) \tag{3.27}$$

$$i\hbar\mathbf{v}_F\nabla v\left(\mathbf{r}\right) + \Delta^*\left(\mathbf{r}\right)u\left(\mathbf{r}\right) = \epsilon v\left(\mathbf{r}\right). \tag{3.28}$$

These equations are significantly easier to handle than the BdG-equations, since they describe a first-order problem.

Consider an incoming particle from the left half-space $x < 0$, travelling towards the superconducting interface at $x = 0$, assuming that both the normal region and the superconductor have the same Fermi velocity v_F. The one-dimensional Andreev equations for the NS interface read

$$-i\hbar v_{F,x}\frac{d}{dx}u\left(x\right) + \Delta(x)v\left(x\right) = \epsilon u\left(x\right) \tag{3.29}$$

$$i\hbar v_{F,x}\frac{d}{dx}v\left(x\right) + \Delta^*(x)u\left(x\right) = \epsilon v\left(x\right). \tag{3.30}$$

In the normal region (for $x < 0$), the superconducting gap parameter decreases to zero on a length scale shorter than ξ_0. Therefore, the step-like approximation from eq. (3.25) holds. In the normal region, the coefficients $u\left(x\right)$ and $v\left(x\right)$ are independent. The ansatz contains an incident wave with unity amplitude and a reflected hole with amplitude r.

$$\Psi_N\left(x\right) = \begin{pmatrix} u\left(x\right) \\ v\left(x\right) \end{pmatrix}_N = e^{ik_N x}\begin{pmatrix} 1 \\ 0 \end{pmatrix} + re^{-ik_N x}\begin{pmatrix} 0 \\ 1 \end{pmatrix}, \tag{3.31}$$

where, writing $v_x \equiv v_{F,x}$,

$$k_N = \frac{\epsilon}{\hbar v_x}. \tag{3.32}$$

In the superconducting region, the solution for the wave function has the form

$$\Psi_S\left(x\right) = \begin{pmatrix} u\left(x\right) \\ v\left(x\right) \end{pmatrix}_S = te^{ik_S x}\begin{pmatrix} u_0 \\ v_0 \end{pmatrix}. \tag{3.33}$$

The expression for the wave vector k_S depends on the energy of the incoming particle, which can be either *above* or *below* the gap.

For high energies *above* the gap, $\epsilon > |\Delta|$, the wave vector is

$$k_S = \frac{\sqrt{\epsilon^2 - \Delta^2}}{\hbar v_x} \tag{3.34}$$

If the energy of the incoming particle is higher than the gap energy, it can be transmitted into the superconductor. The amplitude t therefore is the transmission probability. The coherence factors u_0, v_0 can be found by solving the BdG equations within the BCS framework. Matching the boundary conditions at the interface yields

$$r = \frac{v_0}{u_0}, \quad t = \frac{1}{u_0}. \tag{3.35}$$

Normalizing the wave functions leads to

$$|r|^2 + (u_0^2 - v_0^2)|t|^2 = 1 \tag{3.36}$$

Since ϵ is the energy relative to the Fermi energy, the normal wave vector from eq. (3.31) can be written in terms of

$$\mathbf{q}_\pm = \left(k_F \pm \frac{\epsilon}{\hbar v_F} \right) \hat{\mathbf{k}}_F \tag{3.37}$$

$$\Psi_N (\mathbf{r}) = e^{i\mathbf{q}_+ \cdot \mathbf{r}} \begin{pmatrix} 1 \\ 0 \end{pmatrix} + a e^{i\mathbf{q}_- \cdot \mathbf{r}} \begin{pmatrix} 0 \\ 1 \end{pmatrix}. \tag{3.38}$$

Using eq. (3.37), one can determine the trajectory of the reflected hole to coincide with the trajectory of the incoming electron. The change in momentum,

$$\Delta p_x = -\frac{2e}{v_x}, \tag{3.39}$$

is small. The components p_y, p_z are conserved, therefore the trajectory of the reflected hole is almost the same as the trajectory of the incoming electron.

For energies *below* the gap, $\epsilon < |\Delta|$, there are no states available inside the gap. Therefore, the wave function decays inside the superconductor.

The wave function is

$$\begin{pmatrix} u(x) \\ v(x) \end{pmatrix}_S = t e^{-\tilde{k}_S x} \begin{pmatrix} u_0 \\ v_0 \end{pmatrix}, \tag{3.40}$$

where

$$\tilde{k}_S = \frac{\sqrt{\Delta^2 - \epsilon^2}}{\hbar v_x}. \tag{3.41}$$

For sub-gap energies, the amplitudes of the normal wave functions are slightly modified:

$$r = \frac{\tilde{v}_0}{\tilde{u}_0} \tag{3.42}$$

and

$$\text{and} \quad t = \frac{1}{\tilde{u}_0}, \tag{3.43}$$

where

$$\tilde{u}_0 = \frac{1}{\sqrt{2}} \left(1 + i \frac{\sqrt{|\Delta|^2 - \epsilon^2}}{\epsilon} \right) \quad \text{and} \quad \tilde{v}_0 = \frac{1}{\sqrt{2}} \left(1 - i \frac{\sqrt{|\Delta|^2 - \epsilon^2}}{\epsilon} \right). \tag{3.44}$$

In this case, it holds that

$$|r|^2 = 1 \tag{3.45}$$

In other words, there are no transmitted particles and all particles are Andreev reflected.
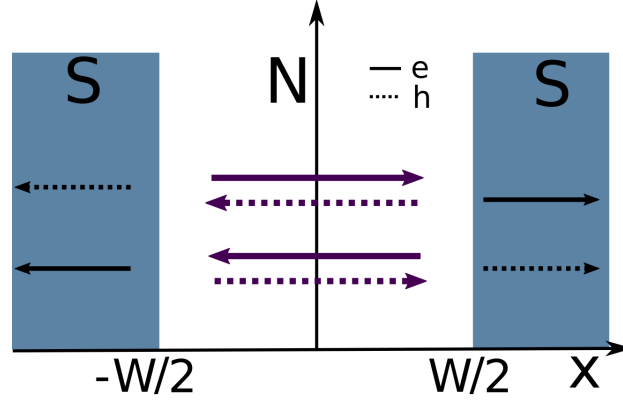
Figure 3.3: *An SNS junction of width W. Electrons are indicated as solid arrows, holes as dashed ones. An electron (hole) is Andreev reflected as a hole (electron) at one side, which then again is reflected at the other side. In this way, Andreev bound states form in the junction.*

3.3 Theory of SNS junction

So far, only NS interfaces have been considered. The same procedure can be applied to superconductor - normal metal - superconductor (SNS) junctions: A sandwich structure of a superconductor on the left side, a normal region in the middle and a superconductor on the right side, as visualized in figure 3.3. At both interfaces, a particle can be Andreev-reflected. Each time an electron is Andreev-reflected at the right side and a hole travels back, a Cooper pair is induced into the right superconductor. In the same manner, a Cooper pair is stolen from the left superconductor when the hole is Andreev-reflected as an electron. This process is illustrated in figure 3.3. As an overall consequence, a supercurrent through the SNS junction can be observed. This process leads to localized electrons with bound states, known as Andreev bound states.

In the following, an SNS junction with normal region at $|x| < W/2$, the right superconductor at $x > +W/2$ and the left superconductor at $x < -W/2$ is considered. The electrons in both superconducting regions and in the normal metal have the same Fermi velocity and there are no insulating barriers between them. This means that W is smaller than the electron mean free path. For short W this implies that the mean free path is larger than the superconducting coherence length. The phase difference between the superconductors is χ, so the right superconductor can be assumed to be characterised by the phase $\chi/2$ and the left one by $-\chi/2$. The semi-classical approximation is used and a wave function with the form

$$\Psi\left(\mathbf{r}\right) = e^{i\mathbf{k_F r}} \begin{pmatrix} u\left(\mathbf{r}\right) \\ v\left(\mathbf{r}\right) \end{pmatrix}. \tag{3.46}$$

is needed. In the normal region, it holds that

$$\Psi_N\left(x\right) = A \cdot \left[e^{ik_N x} \begin{pmatrix} 1 \\ 0 \end{pmatrix} + a e^{-ik_N x} \begin{pmatrix} 0 \\ 1 \end{pmatrix} \right], \tag{3.47}$$

$$k_N = \frac{\epsilon}{\hbar v_x}. \tag{3.48}$$

Assuming that $k_x > 0$, the wave function in the right superconductor $(x > W/2)$ is

$$\Psi_S^R(x) \quad = \quad d_1 e^{-\tilde{k}_S x} \begin{pmatrix} \tilde{u}_0 e^{i\chi/4} \\ \tilde{v}_0 e^{-i\chi/4} \end{pmatrix}, \tag{3.49}$$

$$\tilde{k}_S \quad = \quad \frac{\sqrt{|\Delta|^2 - \epsilon^2}}{\hbar |v_x|}. \tag{3.50}$$

For the left superconductor, the wave function is

$$\Psi_S^L(x) = d_1' e^{\tilde{k}_S x} \begin{pmatrix} \tilde{v}_0 e^{-i\chi/4} \\ \tilde{u}_0 e^{i\chi/4} \end{pmatrix}. \tag{3.51}$$

Applying the continuity condition at the interfaces leads to

$$a e^{-i k_n W} \quad = \quad \frac{\tilde{v}_0}{\tilde{u}_0} e^{-i\chi/2} \tag{3.52}$$

$$a e^{i k_n W} \quad = \quad \frac{\tilde{u}_0}{\tilde{v}_0} e^{i\chi/2}. \tag{3.53}$$

Combining these equations, we find

$$e^{2i(k_N W - \chi/2)} = \frac{\epsilon + i\sqrt{|\Delta|^2 - \epsilon^2}}{\epsilon - i\sqrt{|\Delta|^2 - \epsilon^2}}. \tag{3.54}$$

To simplify this expression, one can introduce

$$\sin \alpha := \frac{\epsilon}{|\Delta|}, \quad -\pi/2 < \alpha < \pi/2 \tag{3.55}$$

Using eq. (3.55), one can rewrite the right hand side of eq. (3.54) in terms of trigonometric functions and gets

$$e^{2i(k_N W - \chi/2)} = e^{-2i\alpha + i\pi}, \tag{3.56}$$

which then leads to

$$\epsilon = \frac{\hbar v_x}{W} \left(\pi \left(l + \frac{1}{2} \right) - \arcsin \frac{\epsilon}{|\Delta|} + \frac{\chi}{2} \right). \tag{3.57}$$

If $k_x < 0$, it holds that

$$\Psi_S^R(x) = d_2 e^{-\tilde{k}_S x} \begin{pmatrix} \tilde{v}_0 e^{i\chi/4} \\ \tilde{u}_0 e^{-i\chi/4} \end{pmatrix} \tag{3.58}$$

For the left superconductor, the wave function is

$$\Psi_S^L(x) = d_2' e^{\tilde{k}_S x} \begin{pmatrix} \tilde{u}_0 e^{-i\chi/4} \\ \tilde{v}_0 e^{i\chi/4} \end{pmatrix} \tag{3.59}$$

An analogous calculation leads to

$$\epsilon = -\frac{\hbar |v_x|}{W} \left(\pi \left(l - \frac{1}{2} \right) + \arcsin \frac{\epsilon}{|\Delta|} + \frac{\chi}{2} \right) \tag{3.60}$$

The final result for the spectrum is

$$\epsilon = \pm \frac{\hbar |v_x|}{W} \left(\pi \left(l \pm \frac{1}{2} \right) \mp \arcsin \frac{\epsilon}{|\Delta|} + \frac{\chi}{2} \right) \tag{3.61}$$

The upper sign is corresponds to $k_x > 0$ and the lower sign corresponds to $k_x < 0$. Normalizing the wave functions fixes the coefficient in eq. (3.31)

$$|A|^2 = \frac{1}{2(W + k_S^{-1})} = \frac{1}{2} \frac{\sqrt{|\Delta|^2 - \epsilon^2}}{\hbar|v_x| + W\sqrt{|\Delta|^2 - \epsilon^2}}. \qquad (3.62)$$

Limit of short junction

For junctions with small width W, such that

$$W \ll \frac{\hbar v_x}{|\Delta|}, \quad \xi \ll W \qquad (3.63)$$

holds, where $\xi_0 \sim \hbar v_F/|\Delta|$ is the coherence length. Then, in eq. (3.54) the term with $e^{2ik_nW} \approx 1$ and the spectrum becomes

$$\epsilon = \mp \cos\frac{\chi}{2}, \quad 0 < \chi < \pi. \qquad (3.64)$$

Limit of long junction

Long junction, $W \gg \xi_0$, it holds that

$$W \gg \frac{\hbar|v_x|}{|\Delta|}. \qquad (3.65)$$

Then the spectrum is given by

$$\epsilon = \pm \frac{\hbar|v_x|}{W}\left(\frac{\chi}{2} - \frac{\pi}{2}\right) + \frac{l\pi\hbar|v_x|}{W}, \qquad (3.66)$$

because $\arcsin\frac{\epsilon}{|\Delta|}$ can be neglected.

3.4 Supercurrent through the SNS junction

Having established the normal wave functions for SNS junctions, the quantum-mechanical current can be calculated. It is given by

$$\mathbf{j} = \frac{e}{m}\left[f_n u_n^*(\mathbf{r})\left(-i\hbar\nabla - \frac{e}{c}\mathbf{A}\right)u_n(\mathbf{r}) + (1 - f_n)v_n(\mathbf{r})\left(-i\hbar\nabla - \frac{e}{c}\mathbf{A}\right)v_n^*(\mathbf{r}) + \text{c.c.}\right], \qquad (3.67)$$

where n labels quantum states and f_n is the corresponding Fermi distribution. As a simplification, $\mathbf{A} = 0$ is considered:

$$\mathbf{j} = -i\hbar\frac{e}{m}\left[f_n u_n^*(\mathbf{r})\nabla u_n(\mathbf{r}) + (1 - f_n)v_n(\mathbf{r})\nabla v_n^*(\mathbf{r}) + \text{c.c.}\right]. \qquad (3.68)$$

For evaluating eq. (3.67), the normal wave functions from eq. (3.47) are used. In the semi-classical approximation, only the derivatives of the rapidly varying functions $e^{i\mathbf{k}\mathbf{r}}$ contribute to the current, which then reduces to

$$I_x = -\frac{e}{\hbar}\sum_n (1 - 2f_n)\frac{\hbar v_x\sqrt{|\Delta^2| - \epsilon_n^2}}{\hbar v_x + W\sqrt{|\Delta|^2 - \epsilon^2}}. \qquad (3.69)$$

3.5 Specular Andreev reflection, graphene specifics

An unusual form of Andreev reflection has been found at graphene - superconductor interfaces [**?**]. The previously discussed Andreev reflection changes the direction of the incoming particle such that the reflected particle travels on approximately the same trajectory as the incoming one (see section 3.2). This process is called Andreev retro reflection and is illustrated in figure 3.4 b. It is only an approximation, because due to its condensation into a cooper pair, the particle will lose energy during the reflection process. In most metals, hardly any energy loss is observed because the Fermi energy of most metals is large compared to the superconducting energy gap, $E_F \gg \Delta$ [**?**]. Graphene, however, is a semi-metal with low E_F, where the regime with $E_F < \Delta$ is achievable. As a consequence, the E_F dependence of Andreev reflection can be studied in graphene. The single-particle Hamiltonian for graphene is the Dirac Hamiltonian

$$H = \begin{pmatrix} H_+ & 0 \\ 0 & H_- \end{pmatrix}, \tag{3.70}$$

where

$$H_\pm = i\hbar \left(\sigma_x \delta_x \pm \sigma_y \delta_y \right) + U. \tag{3.71}$$

For the expression of $H_\pm$, the pauli matrices σ_i have been used. An electrostatic potential, $U(\mathbf{r})$, can be present in the sample. Here, it is chosen such that

$$U(\mathbf{r}) = -U_0 \theta(x) \tag{3.72}$$

This modifies the BdG equation, resulting in

$$\begin{pmatrix} H_\pm + E_F & \Delta \\ \Delta^* & E_F - H_\pm \end{pmatrix} \begin{pmatrix} u \\ v \end{pmatrix} = \epsilon \begin{pmatrix} u \\ v \end{pmatrix}, \tag{3.73}$$

where the electron spinor has two components $\left(u_1, u_2 \right) = \left(\Psi_{A+}, \Psi_{B+} \right)$, and the hole spinor is $\left(v_1, v_2 \right) = \left(\Psi_{A-}^*, \Psi_{B-}^* \right)$. Eq. (3.73) leads to the energy spectrum

$$\epsilon = \sqrt{|\Delta|^2 + \left(E_F - U \pm \hbar v |\mathbf{k}| \right)^2}, \tag{3.74}$$

with

$$|\mathbf{k}| = \sqrt{k_x^2 + k_y^2}. \tag{3.75}$$

The dispersion relation has four solutions for $\mathbf{k}$. Two of them lead to a positive velocity $v_x = \hbar^{-1} d\epsilon dk_x$ corresponding to each one electronic and one hole excitation. A reflected hole can be in one of the following two states: It is reflected either into the conduction band with $\epsilon < E_F$ (retro reflection) or into the valence band with $\epsilon > E_F$ (specular reflection). Specular reflection is the dominating process, when the Fermi energy is smaller than the gap energy, $E_F \ll \Delta$. For $E_F \gg \Delta$, the retro reflection dominates.
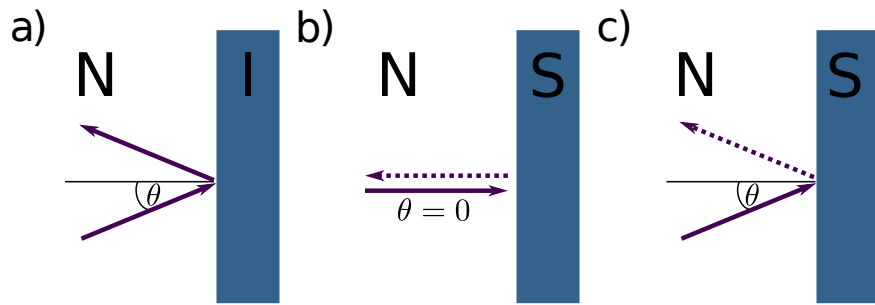
Figure 3.4: *Reflection processes. Solid arrows represent electrons, dashed arrows represent holes.*
a) Specular reflection of an electron at an insulating interface (I).
b) Andreev retro reflection of an electron with into a hole.
c) Specular Andreev reflection of an electron into an hole with incident angle $\theta \neq 0$.

4 Analytical Model

4.1 Foundation of the quasiclassical model

From section 3.3 it is known that Andreev reflection of electrons in a SNS junction leads to Andreev bound states within the junction. Each one of these bound states contributes to the total current through the junction. Essentially, a bound state can be expressed as a trajectory from one superconductor through the normal metal to the other superconductor. The superconducting current density is found through geometrical analysis of possible trajectories. The total current density is then found by adding up all these trajectories. The two dimensional junction (schematic
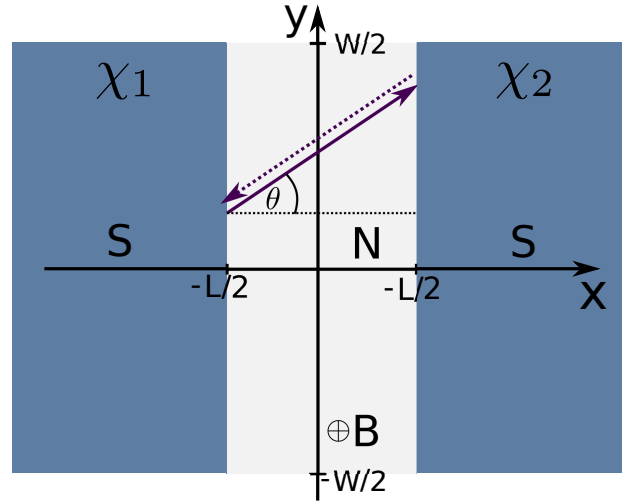

Figure 4.1: *SNS junction with width W and length L. A trajectory connecting the interfaces is parametrized by the angle θ between the trajectory and the x-axis. χ_1 and χ_2 are the superconducting phases, with total phase differece $\chi = \chi_2 - \chi_1$.*

shown in fig 4.1) is a short and wide junction with width W and length L, where $W \gg L$. The NS-interfaces are parallel to the y-axis and are placed at $x = \pm L/2$. Each of the superconducting leads has a phase χ_1 and χ_2, and the overall phase difference is $\chi = \chi_1 - \chi_2$. The superconducting gap parameter Δ is only present in the superconducting leads. Close to the interface, Δ begins to decay on a length scale of the superconducting coherence length ξ_0 into the normal region. Similar to the procedure in section 3.3, this decay is neglected and a step-like behaviour is assumed for the superconducting gap parameter:

$$\Delta (x) = |\Delta|e^{\chi_1}\Theta\left(-L/2 - x\right) + |\Delta|e^{\chi_2}\Theta\left(x - L/2\right). \tag{4.1}$$

The thermal length scale of the system assumed to be larger than the sample length:

$$L_T = \hbar v_F / k_B T \gg L. \tag{4.2}$$

The transport through the junction is assumed to be ballistic, resulting in the trajectories being straight and not being altered by scattering in the normal region. However, the presence of the magnetic field in the normal region of the sample will lead to a bending of the trajectories due to the Lorentz force. Depending on the strength of magnetic field B and the Fermi velocity, the radius of this curve is

$$r_B = \frac{m v_F}{e B} \tag{4.3}$$

In order to justify the assumption of straight trajectories, either the magnetic field has to be weak enough, or the Fermi velocity (wavelength) has to be large (short) enough. Then, the cyclotron radius r_B is larger than the sample size L, and straight trajectories are a valid assumption.

4.2 Plane setup: calculation of current

Summing up the contributions leads to the current through the SNS junctions, the Josephson current $J(\chi)$, which is a function of the superconducting phase difference $\chi = \chi_2 - \chi_1$. By maximizing the Josephson current with respect to χ, one finds the critical current I_c.

A trajectory connecting the two superconducting interfaces can be parametrized by the angle θ between the trajectory and the x-axis. For a trajectory from a point $(-L/2, y_1)$ to another at $(+L/2, y_2)$, the angle for the parametrization is

$$\tan \theta = \frac{y_2 - y_1}{L}. \tag{4.4}$$

Figure 4.1 visualizes this parametrization. Several papers outline approaches to this problem ([7], [8]) and are based on the same concept. The Josephson current in [7] has the form

$$J = \frac{2e}{\pi L} \sum_{\boldsymbol{\kappa}} v_{Fx}^{\boldsymbol{\kappa}} \mathcal{J}(\chi), \tag{4.5}$$

where $\boldsymbol{\kappa}$ is the tangential momentum with $\boldsymbol{\kappa}^2 + \mathbf{k_x}^2 = k_F^2$. v_{Fx} is the projection of v_F on the x-axis

$$v_{Fx} = v_F \cos \theta \tag{4.6}$$

and $\mathcal{J}(\chi)$ is the current density. A similar ansatz to eq. (4.5) is described in [9]:

$$J = \int_{-W/2}^{+W/2} dy \int_{-p_F}^{+p_F} \frac{dp_y}{2\pi} \cos \theta \mathcal{J}(\chi, \phi). \tag{4.7}$$

For a fixed point at the left interface, the current density is integrated over all possible momenta. This integral can be expressed through the endpoints of a trajectory. The integration over p_y can then be replaced by $p_y = p_F \sin \theta \to dp_y/d\theta = p_F \cos \theta$. The integration over the angle θ can be substituted by the integration over y_2, a point at the right interface. The result for the Josephson current reads

$$J(\chi, \phi = 0) = \frac{2 e v_F}{\pi \lambda_F L^2} \int \int_{-W/2}^{W/2} dy_1 dy_2 \frac{\mathcal{J}(\chi)}{\left[1 + \left(\frac{y_1 - y_2}{L} \right)^2 \right]^2}. \tag{4.8}$$

By maximizing the Josephson current with respect to χ, the critical current can be found as:

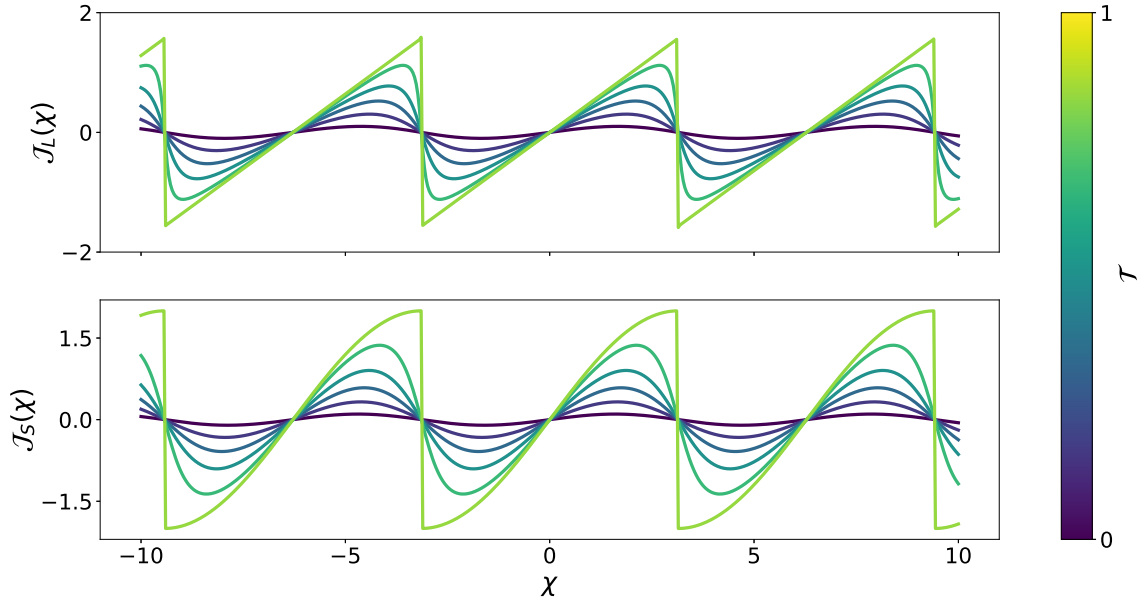$$I_c(\phi) = \max_{\chi} \left\{ J(\chi, \phi) \right\}. \tag{4.9}$$

Figure 4.2: *Current density plotted against the superconducting phase difference $\chi = \chi_2 - \chi_1$. The density from eq. (4.11) gives the sawtooth like shape for $\mathcal{J}^l$ for high values of $\mathcal{T}$. In the short junction limit, $\mathcal{J}^s$ holds from eq. (4.10). For low values of the transmission coefficient $\mathcal{T}$, both current densities look similar (sinusoidal form).*

The current density $\mathcal{J}$ depends on the ratio of W and L. For $W \gg L$, the junction is a short junction, while for $W \ll L$, it is a long junction. In the short junction limit, the current density is calculated in [10]

$$\mathcal{J}^s(\chi) = \frac{\mathcal{T}_n \sin \chi}{\sqrt{1 - \mathcal{T}_n \sin^2 \frac{\chi}{2}}} \tag{4.10}$$

which can be derived in the framework of the scattering matrix formalism. $\mathcal{T}_n$ is the transmission coefficient for a given conducting channel. For low transmission, $\mathcal{T} \ll 1$, only the first addend contributes, which leads to the conventional Josephson relation $J \simeq \mathcal{T} \sin \chi$.
For the long junction, from [8] the following expression can be found:

$$\mathcal{J}^l(\chi) = \sum_{k=1}^{\infty} \frac{(-1)^{k+1}\mathcal{T}^k}{k} \sin(k\chi). \tag{4.11}$$

The coefficient $\mathcal{T}$ has been included phenomenologically in this formula and includes the normal scattering in the sample. Figure 4.2 shows a plot of both short and long junction limit current densities. For $\mathcal{T} \ll 1$, $\mathcal{J}^s$ takes a sinusoidal form, which also true for the long junction limit. For each of those, the classical Josephson relation can be found in the limit of low transmissions:

$$\mathcal{J} \simeq \mathcal{T} \sin \chi \tag{4.12}$$

The current densities differ for a large transmission coefficient $\mathcal{T} \simeq 1$: A sawtooth-like shape is observed in the long junction limit, and in the short junction limit, a sinusoidal shape appears.

Including magnetic field

Up to this point, the current has been derived for zero magnetic field. If a finite magnetic field is considered, the phase χ is modified because of two effects: First, the magnetic phase that will be acquired along a trajectory connecting two points y_1 and y_2 leads to an additional term in the phase. Also, the superconducting phases at each interface become functions of $y_{1/2}$ (see [9]):

$$\chi_{1/2} = \mp \frac{1}{2}\left(\chi - \frac{2\pi BL}{\phi_0}y_{1/2}\right) \tag{4.13}$$

$$\tilde{\chi}(y_1, y_2) = \chi_2 - \chi_1 \tag{4.14}$$

$$= \chi - \frac{\pi BL}{\phi_0}(y_1 + y_2) \tag{4.15}$$

Assuming that the London penetration depth is small to zero in the superconducting regions, the following gauge for the vector potential can be used:

$$\mathbf{A} = A_y \mathbf{e}_y, \quad A_y = \begin{cases} -Bx, & -L/2 \le x \le L/2, \\ -\frac{1}{2}BL|x|, & |x| > L/2 \end{cases} \tag{4.16}$$

This gauge will give no additional contribution to the phase on straight trajectories

$$\delta\chi = \frac{2\pi}{\Phi_0}\int d\mathbf{l} \cdot \mathbf{A} \tag{4.17}$$

$$= \frac{2\pi}{\Phi_0}\int_{-L/2}^{L/2} \frac{dx}{\cos\theta}A_y(x)\sin\theta \tag{4.18}$$

$$= -\frac{2\pi B}{\Phi_0}\frac{y_2 - y_1}{L}\int_{-L/2}^{L/2} x dx \tag{4.19}$$

$$= 0, \tag{4.20}$$

where eq. (4.4) has been used. The total phase for this setup is therefore eq. (4.15). This results in the current phase relation in the expression for the Josephson current from eq. (4.8) to be replaced by the effective phase $\chi \to \tilde{\chi}(y_1, y_2)$:

$$J\left(\chi, \phi\right) = \frac{2ev_F}{\pi\lambda_F L^2}\int\int_{-W/2}^{W/2} dy_1 dy_2 \frac{\mathcal{J}(\tilde{\chi}(y_1, y_2))}{\left[1 + \left(\frac{y_1 - y_2}{L}\right)^2\right]^2} \tag{4.21}$$

Here, the expression for the supercurrent density in the long junction limit and in the limit of low transmission, eq. (4.12) is used. Plugging in the effective phase from eq. (4.15), the Josephson current reads

$$J(\tilde{\chi}(y_1, y_2), \phi) = \mathcal{T}\sin\chi\frac{2ev_F}{\pi\lambda_F L^2}\int\int_{-W/2}^{W/2} dy_1 dy_2 \frac{\cos\left(\frac{\pi\phi}{W}(y_1 + y_2)\right)}{\left[1 + \left(\frac{y_1 - y_2}{L}\right)^2\right]^2}, \tag{4.22}$$

where $\sin\tilde{\chi}$ has been rearranged in term of trigonometric functions. Since the integration is symmteric in the limits, only the term with $\cos\left(\frac{\pi\phi}{W}(y_1 + y_2)\right)$ is being kept in the expression for the current. Maximizing the Josephson current with respect to χ gives $\sin\chi \to 1$. Evaluating the integration over y_1 and y_2, the critical current is **TODO cite!** found

$$I_c(\chi) = \frac{2eWv_F}{\lambda_F L}\frac{(1 - \{\phi\})\{\phi\}}{|\phi|}, \tag{4.23}$$
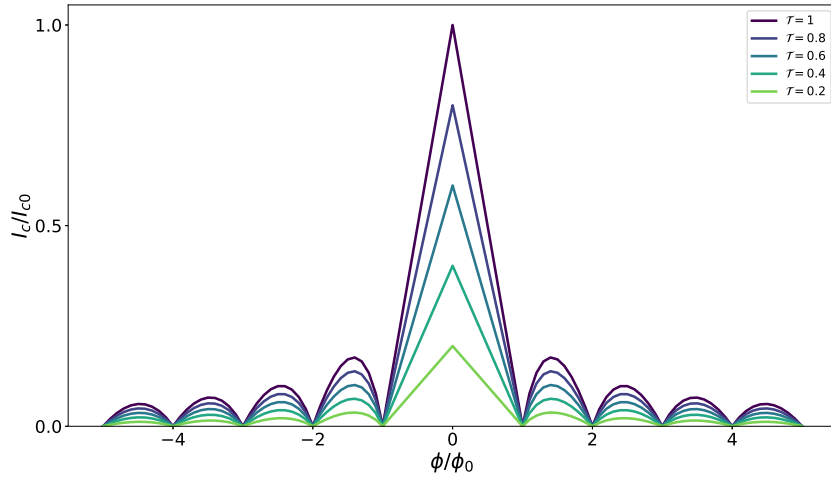
where $\mathcal{T} \approx 1$.

Figure 4.3: *I_c vs. ϕ for different values of $\mathcal{T}$*

Including scattering at the boundaries

So far, straight trajectories connecting the two superconducting interfaces have been considered. A process that is possible in principal, is a trajectory of an electron that is scattered at a side boundary (see figure **TODO!**). It is clear that, especially in the case of a short and wide junction with $W \gg L$, these trajectories do not contribute as much as the straight trajectories. When a trajectory is scattered at, say, a point at the upper edge $(x, y) = (x_s, pW/2)$, the parametrisation for the angle describing the trajectory is

$$\tan\theta = \frac{\bar{y}_2 - y_1}{L} = \frac{W - y_2 - y_1}{L}. \tag{4.24}$$

In this parametrisation, the coordinate $\bar{y}_2$ is the mirror image of y_2. For straight trajectories the vector potential **A** does not give an additional contribution, which can be seen in eq. (**??**). The effective phase is in this case determined by eq. (4.15). When considering the scattering at side boundaries with the parametrization from eq. (4.24), the contribution from the magnetic phase is no longer zero,

$$\delta\chi = \frac{2\pi}{\Phi_0} \int_{-L/2}^{x_s} dx A_y(x) \tan\theta - \frac{2\pi}{\Phi_0} \int_{x_s}^{+L/2} dx A_y(x) \tan\theta \tag{4.25}$$

$$= -\frac{2\pi B}{\Phi_0} \tan\theta \left(\int_{-L/2}^{x_s} x\, dx - \int_{x_s}^{+L/2} dx \right) \tag{4.26}$$

$$= -\frac{2\pi B}{\Phi_0} \tan\theta \left(x_s^2 - (L/2)^2 \right) \tag{4.27}$$

$$= \frac{\pi\phi}{2W} \frac{(W - 2y_1)(W - 2y_2)}{W - y_1 - y_2}, \tag{4.28}$$

since the trajectory changes the direction and therefore $d\mathbf{l} \cdot \mathbf{A}$ changes sign. The total effective phase difference is then, using eq. (4.15)

$$\tilde{\chi}(y_1, y_2) = \chi - \frac{\pi\phi}{2W} \left(2(y_1 + y_2) - \frac{(W - 2y_1)(W - 2y_2)}{W - y_1 - y_2} \right) \tag{4.29}$$
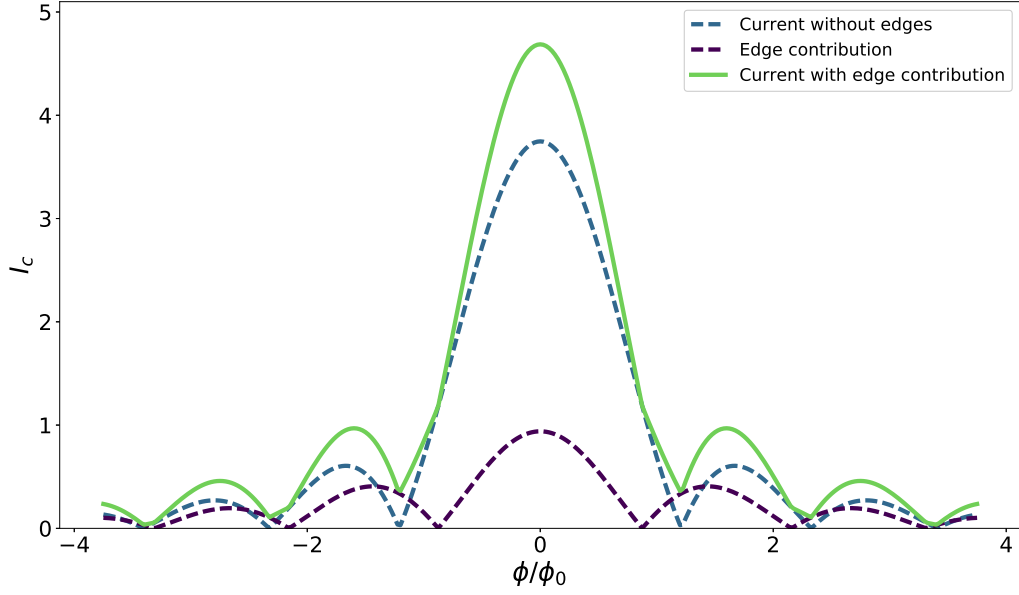
Figure 4.4: *Comparison of different contributions to the current at $\mathcal{T} = 1$.*

With the contribution from side boundary scattering, the total Josephson current is

$$J\left(\chi, \phi\right) = J^{(0)}\left(\chi, \phi\right) + 2J^{(1)}\left(\chi, \phi\right). \tag{4.30}$$

$J^{(0)}$ denotes the part coming from straight trajectories. Since there are two side boundaries, the part describing the scattering, $J^{(1)}$, has an additional factor 2 and reads

$$J^{(1)} = \frac{2ev_F}{\pi\lambda_F L^2} \int \int_{-W/2}^{W/2} \frac{dy_1 dy_2}{\left[1 + \left(\frac{y_1 - y_2}{L}\right)^2\right]^2} \mathcal{J}\left(\chi - \frac{\pi\phi}{2W}\left(2(y_1 + y_2) - \frac{(W - 2y_1)(W - 2y_2)}{W - y_1 - y_2}\right)\right) \tag{4.31}$$

This contribution has not been noted in [9]. In the case of short and wide junctions, it is sufficient to consider only $J^{(0)}$. For the cases, when $W/L \simeq 1$, it is necessary to sum over all possible edge channels. Figure 4.4 shows the result of equations (4.31) and (4.22). The overall contribution from the side scattering is lower than the contribution of only straight trajectories. In the total current, eq. (4.30), the edge scattering manifests by lifting the minimas from zero (see green curve in figure 4.4). This is in agreement with the results from [9]

4.3 Calculation of QPC current

The quasi classical formalism can even be employed to modified SNS junctions. One can build gates on top of the normal region of the junction in a way that the current cannot pass through the gated regions (see chapter 2). In the quasi classical picture, this means that the possibilities for trajectories connecting two points at the superconducting interfaces are limited through the geometry of the constriction.

Figure 4.5 shows a sketch of the quantum point contact set-up which will be analysed with the
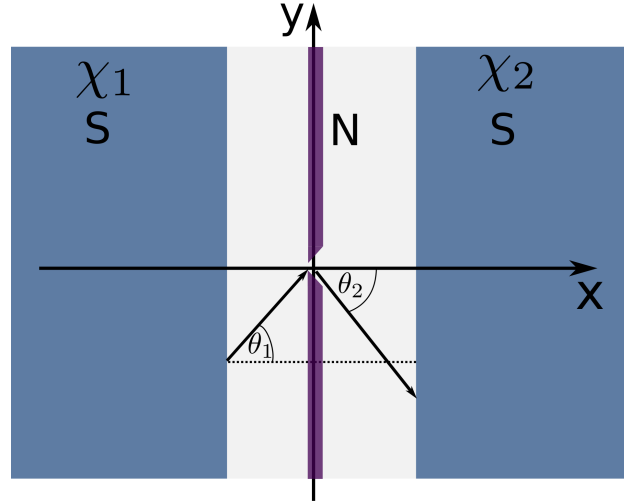
Figure 4.5: *SNS junction with a QPC gate on top. The split is located at $(x, y) = (0, 0)$ and the width of the barrier is assumed to be negligible. Each trajectory that contributes has to pass though the origin. The angles θ_1 and θ_2 parametrize this trajectory.*

quasi classical formalism. The normal region of the SNS junction is covered by a gate with a small split in the middle. The split is located at $(x, y) = (0, 0)$ so that the sample is symmetric around the origin. The width of the split is in the order of λ_F and can thereby be viewed as an isotropic scattering point with transmission coefficient $\mathcal{T}_0$. Trajectories connecting the two superconducting interfaces have to pass through the QPC. For simplicity, the geometrical width of the barrier is neglected, only straight trajectories are considered, and scattering at side edges is neglected. This modified set-up leads to a different parametrization of the trajectories and therefore to a different magnetic phase than in eq. (4.15).

With the QPC set-up, all possible trajectories are parametrized by two angles θ_1 and θ_2. θ_1 describes the trajectory before passing through the QPC in the region $-L/2 < x < 0$, and θ_2 after passing through the QPC. The parametrization of the trajectories reads

$$\tan \theta_1 = -\frac{2y_1}{L}, \quad \tan \theta_2 = \frac{2y_2}{L} \tag{4.32}$$

With the gauge from eq. (4.16), the magnetic phase acquired within the sample reads

$$\frac{2\pi}{\Phi_0} \int d\mathbf{l} \cdot \mathbf{A} \;=\; -\frac{\pi B}{\Phi_0} \left(\frac{L}{2} \right)^2 \left(-\tan \theta_1 + \tan \theta_2 \right) = -\frac{\pi \phi (y_1 + y_2)}{2W}. \tag{4.33}$$

The total phase difference is the difference of the contribution coming from the magnetic field, eq. (4.33) and the supcondcucting phase difference eq. (4.15). The effective phase for the QPC setup is found to be

$$\tilde{\chi}(y_1, y_2) = \chi - \frac{\pi \phi}{2W}(y_1 + y_2). \tag{4.34}$$

One consequence of the additional gate on top of the normal region is the change in the effective phase, resulting in a modified current phase relation $\mathcal{J}(\tilde{\chi}(y_1, y_2))$. Another consequence is a modified expression for the critical current. In the set-up without gates, straight trajectories with a fixed angle θ were considered and summed up to a total contribution. The difference in the QPC set-up is the split in the gate, which is modelled as an isotropic scattering point. The trajectories being summed up in this set-up can be thought to consist of two parts. The first part connects y_1
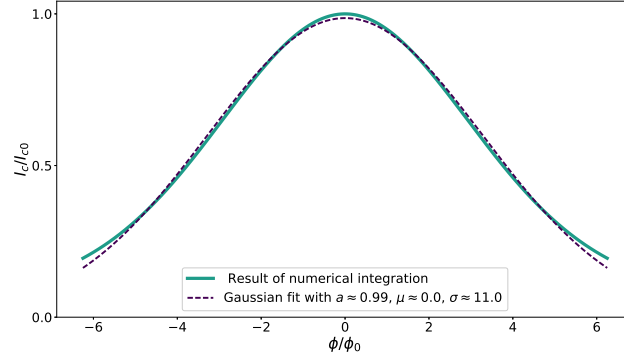
with the split at $(x, y) = (0, 0)$ and is determined by the direction of the trajectory. This explains the Fermi velocity in this part(?). The second part of the current trajectory starts from the origin and connects it with a point at the right interface y_2. Summing up, the critical current in the QPC set-up is

$$I_c^{\text{QPC}}(\phi) \propto \max_\chi \int d\theta_1 v_F \cos^2 \theta_1 \int d\theta_f \cos \theta_f \mathcal{J} \left(\tilde{\chi}(\theta_1, \theta_2) \right) \tag{4.35}$$

The QPC is modelled as an isotropic scatterer with transmission probability $\mathcal{T}$. If the transmission is small, $\mathcal{T} << 1$, eq. (4.12) can be used for $\mathcal{J}$. The angles $\theta_{1,2}$ can be rewritten in terms of $y_{1,2}$ by using the parametrization from eq. (4.32), allowing the normalized critical current to be expressed as

$$\frac{I_c(\phi)}{I_c(0)} = \frac{\mathcal{I}_2(\phi)\mathcal{I}_{3/2}(\phi)}{\mathcal{I}_2(0)\mathcal{I}_{3/2}(0)}, \tag{4.36}$$

where the integrals $\mathcal{I}$ are defined as

$$\mathcal{I}_k(\phi) = \frac{2}{L} \int_{-W/2}^{+W/2} dy \frac{\cos\left(\frac{\pi \phi y}{2W}\right)}{\left[1 + \left(\frac{2y}{L}\right)^2\right]^k} \tag{4.37}$$

Numerical evaluation

Evaluating the integral numerically, one finds

Evaluation in limits

The current can be evaluated in the limit of small flux $\phi \to 0$, and in limit of high fields $\phi \to \infty$. At $\phi = 0$ the cosine term becomes one leading to the simple expression

$$\mathcal{I}_2(0)\mathcal{I}_{3/2}(0) = \frac{2W^2 L}{\left(L^2 + W^2\right)^{3/2}} + \frac{2W}{\sqrt{L^2 + W^2}} \arctan \frac{W}{L} \tag{4.38}$$

$$\equiv \frac{2x^2}{\left(1 + x^2\right)^{3/2}} + \frac{2x}{\sqrt{1 + x^2}} \arctan x, \tag{4.39}$$
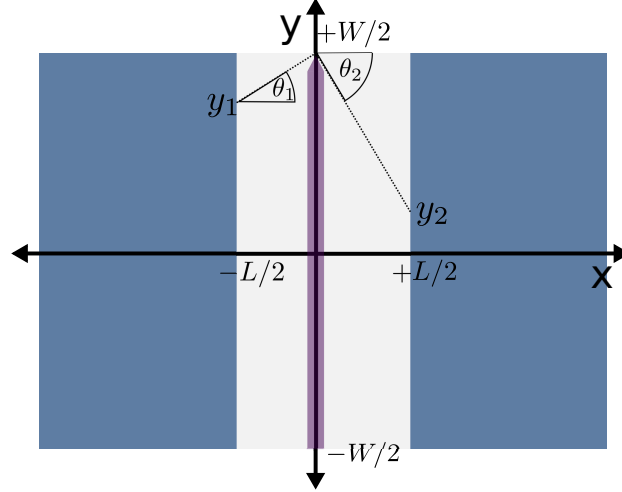
Figure 4.6: *A SNS junction with split at upper edge, $(x, y) = (0, +W/2)$. Similar to the QPC set-up, this constriction is formed in a way that each trajectory has to pass through to contribute to the current.*

where $x \equiv W/L$. The parabolic asymptotics of the critical current at small ϕ is found by expanding the cosine factors in the numerator:

$$\frac{I_c(\phi)}{I_{c0}} \simeq 1 - \frac{\pi^2 \phi^2}{32} f_0(W/L) \tag{4.40}$$

$$f_0(x) = \frac{\sqrt{x^2 + 1} \log\left(\sqrt{x^2 + 1} + x\right)}{x^3} - \frac{2}{x(x + (x^2 + 1)\arctan x)} \tag{4.41}$$

In the opposite limit of high fields, $\phi \to \infty$, the integration in eq. (4.37) is extended over y_1 and y_2 to $\pm\infty$ and obtain

$$\frac{I_c(\phi)}{I_{c0}} = \frac{\pi^{3/2}}{8x} \frac{(1 + x^2)^{3/2}}{x + (1 + x^2)\arctan x} \left(\frac{\pi\phi}{2x}\right)^{3/2} \exp\left(-\frac{\pi\phi}{2x}\right) \tag{4.42}$$

4.4 QPC edge current

Additionally to the QPC, two edge channels at $(x, y) = (0, \pm w/2)$ are introduced. The QPC is modelled with the transmission coefficient $\mathcal{T}_q$, and the edge channel with the coefficient $\mathcal{T}_e$. The lattice orientation of the graphene structure may may be either predominantly arm-chair or zigzag. Depending on this orientation, the edge currents may or may not contribute significantly to the total current. The Fraunhofer pattern changes accordingly. The parametrization of an edge trajectory, illustrated in figure **??**, reads

$$\tan\theta_1 = \frac{W - y_1}{L/2}, \quad \tan\theta_2 = -\frac{W - y_2}{L/2}. \tag{4.43}$$

Similar to the QPC contribution, the magnetic phase gain along the trajectory is calculated. For the upper edge, the result is

$$\frac{2\pi}{\phi_0} \int d\mathbf{l} \cdot \mathbf{A} = \frac{2\pi}{\phi_0} \left(\int A_y(x)|d\mathbf{l}||\mathbf{e_y}|\sin\theta_1 + \int A_y(x)|d\mathbf{l}||\mathbf{e_y}|\sin\theta_2 \right) \tag{4.44}$$

$$= -\frac{2\pi B}{\phi_0} \left(\int_{-L/2}^{0} x dx \tan\theta_1 + \int_{0}^{L/2} x dx \tan\theta_2 \right) \tag{4.45}$$

$$= -\frac{\pi B}{\phi_0} \frac{L}{2} \left(-\tan\theta_1 + \tan\theta_2 \right) \tag{4.46}$$

$$= -\frac{\pi B}{\phi_0} \frac{L}{2} \left(-2W + (y_1 + y_2) \right) \tag{4.47}$$

$$= \pi\Phi - \frac{\pi\Phi}{2W}(y_1 + y_2), \tag{4.48}$$

where

$$\Phi = \frac{\phi}{\phi_0}, \quad \phi = BWL \tag{4.49}$$

has been used. Together with the contribution from the set-up without any constriction from eq. (4.15), the total phase for the edge transmission is added up to

$$\tilde{\chi}(y_1, y_2) = \chi - \frac{3\pi\Phi}{2\phi_0}(y_1 + y_2) + \pi\Phi. \tag{4.50}$$

This is the effective phase $\tilde{\chi}(y_1, y_2)$ for the upper edge. Analogously, the phase for the lower edge can be constructed with a simple sign change in the parametrization in eq. (4.43), leading to

$$\tilde{\chi}(y_1, y_2) = \chi + \frac{3\pi\Phi}{2\phi_0}(y_1 + y_2) - \pi\Phi \tag{4.51}$$

The Josephson relation for the edge contribution has the modified phase from eq. (4.51). The result for the QPC in the limit in high fields, eq. (??), has a transmission coefficient $\mathcal{T} = 1$. For easier comparison with the edge channel contribution, this is rewritten into the following form

$$I_c^{\mathrm{QPC}} = \mathcal{T}_q F(W/L) \tag{4.52}$$

, where the function $F(W/L)$ represents the result from eq. (4.42). The integrals for the upper edge can be written in a similar way:

$$I_c^e = \mathcal{T}_e \sin\left(\chi_0 - \pi\Phi\right) \int_0^\infty d\tilde{y}_1 \int_0^\infty d\tilde{y}_2 \frac{\cos\left(\frac{3\pi\Phi\tilde{y}_1}{2W}\right)}{\left(1 + \left(\frac{2\tilde{y}_1}{L}\right)^2\right)^2} \frac{\cos\left(\frac{3\pi\Phi\tilde{y}_2}{2W}\right)}{\left(1 + \left(\frac{2\tilde{y}_1}{L}\right)^2\right)^{3/2}} \tag{4.53}$$

$$= \mathcal{T}_e \sin\left(\chi_0 - \pi\Phi\right) \frac{F(W/L)}{4}, \tag{4.54}$$

where

$$\tilde{y}_{1/2} = W/2 - y_{1/2} \tag{4.55}$$

The total critical current though the junction is proportional to the sum of the individual contributions

$$\frac{I_c(\phi)}{I_{c0}} = \max_\chi \left\{ \mathcal{T}_q \sin\chi + \frac{\mathcal{T}_e}{4}\sin\left(\chi - \pi\phi\right) + \frac{\mathcal{T}_e}{4}\sin\left(\chi + \pi\phi\right) \right\} / \left(\mathcal{T}_q + \mathcal{T}_e/2 \right) \tag{4.56}$$

$$= \frac{\mathcal{T}_q/\mathcal{T}_e + \cos\left(\pi\phi\right)/2}{\mathcal{T}_q/\mathcal{T}_e + 1/2} \tag{4.57}$$
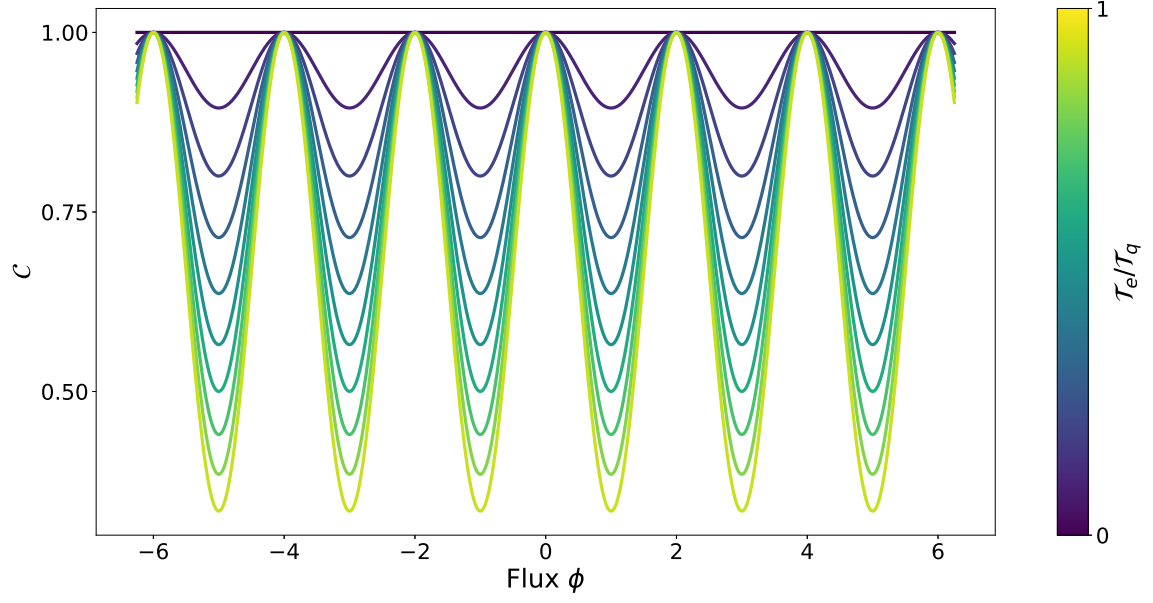
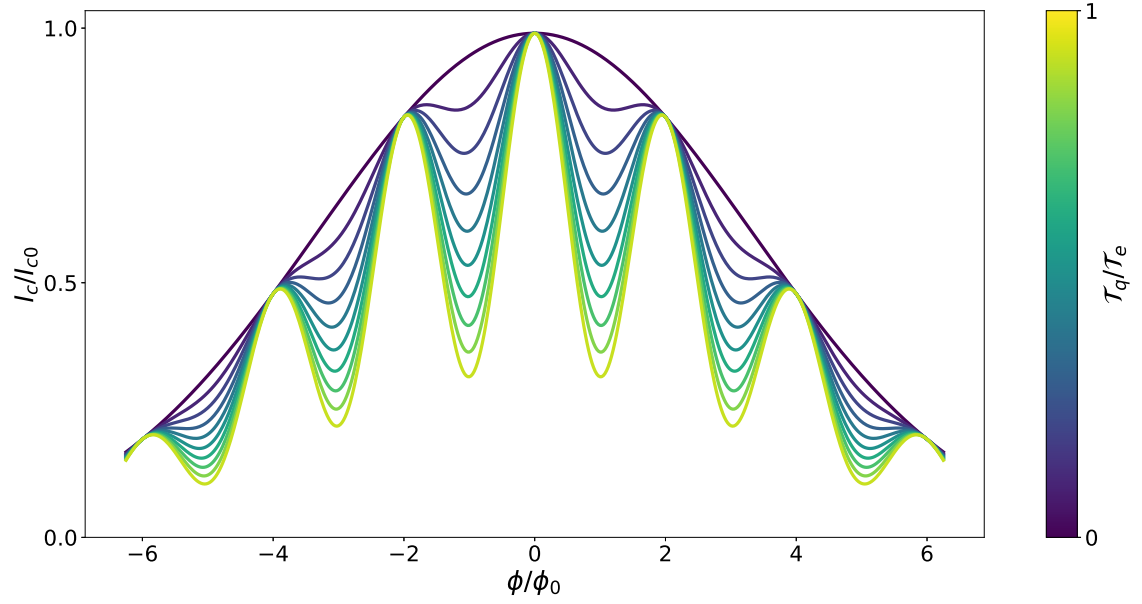**Figure 4.7:** *Another figure caption. Whatever.*
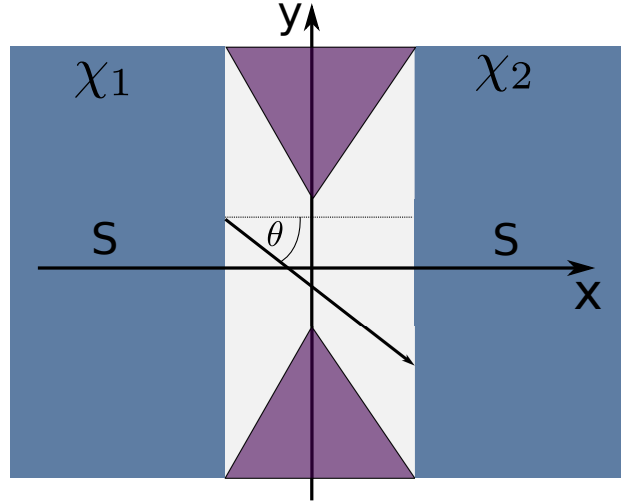

Figure 4.8: *Some figure.*

Figure 4.9: *Hourglass setup*

The result of eq. (4.57) is plotted in figure 4.7. Figure 4.8 shows a plot of the ratio from eq. (4.57) multiplied with a gaussian curve.

TODOs:
make plot colors uniform
add figure captions
check plots for edge current −¿ cbar seems wrong

4.5 Barrier with finite split width - Transition to QPC setup

The QPC setup and the SNS setup without barriers can be linked conceptually by investigating an hourglass-shaped setup. This setup constricts the trajectories through a split with a finite width w_s and is visualized in figure (4.9). When considering only straight trajectories, this split width models the transition to the QPC in the limit of $w_s \to 0$. The difference to the QPC is simply the parametrization of the angles: with a finite w_s, trajectories are parametrized by only one angle θ, the direction does not change after passing the split. When w_s is small enough, like in the QPC case, two independent trajectories are considered with two parametrization angles θ_1 and θ_2. This setup is particularly interesting because the impact of asymmetry in the junction can be studied. When relocating the split by for example moving it along the x-axis, the possible trajectories are limited. As a consequence, the Fraunhofer pattern changes.

5 A framework for the numerical model

5.1 Tight binding model for graphene

Tight binding models are simple, yet powerful methods to calculate the electronic band structure of a system consisting of many lattice sites. Each lattice site is represented in the Hamiltonian as an atomic potential. The basic premise is that the solution to the Schrödinger equation of the isolated system, an electron at a specific site in an atomic potential, is known. The wave function of this electron interacting with the whole lattice (interacting with all other atomic potentials from the other lattice sites) can be constructed from the overlap of the atomic wave functions. Following the notation in [11] and also from [12], the atomic orbital is denoted with ϕ_m. This is the orbital of an atom for unit cell index m, where $m = 1, \dots M$. From these orbitals ϕ_m, a Bloch state Φ_m is constructed. This Bloch state then represents the lattice symmetry (vertauscht mit dem Translationsoperator).

$$\Phi_m\left(\mathbf{k}, \mathbf{r}\right) = \frac{1}{\sqrt{N}} \sum_{i=1}^{N} e^{i\mathbf{k}\mathbf{R}_{m,i}} \phi_m\left(\mathbf{r} - \mathbf{R}_{m,i}\right) \tag{5.1}$$

$\Phi_m\left(\mathbf{k}, \mathbf{r}\right)$ is the Bloch state, the index i labels the unit cell, with $i = 1, \dots N$ (for each unit cell there are M orbitals). $\mathbf{R}_{m,i}$ is the position vector of orbital m in unit cell i. Using this new state, the electronic wave function can be expressed as a linear combination of these orbitals

$$\Psi_j\left(\mathbf{k}, \mathbf{r}\right) = \sum_{m=1}^{M} \psi_{j,m}\left(\mathbf{k}\right) \Phi_m\left(\mathbf{k}, \mathbf{r}\right) \tag{5.2}$$

with coefficients $\psi_{j,m}$. The energy of the Hamiltonian $\mathcal{H}$ is given by

$$E_j\left(\mathbf{k}\right) = \frac{\langle \Psi_j | \mathcal{H} | \Psi_j \rangle}{\langle \Psi_j | \Psi_j \rangle} \tag{5.3}$$

the coefficients can be found by minimising E_j. Introducing the transfer integral matrix H and the overlap integral matrix S, one can write

$$H\psi_j = E_j S_j \psi_j \tag{5.4}$$

The coefficients of the transfer matrix and the overlap matrix are given by

$$H_{m,m'} = \langle \Phi_m | \mathcal{H} | \Phi_{m'} \rangle \tag{5.5}$$

$$S_{m,m'} = \langle \Phi_m | \Phi_{m'} \rangle \tag{5.6}$$

So, in order to find the band energies E_j, these coefficients $H_{m,m'}$ and $S_{m,m'}$ need to be determined. Once they have been calculated, the energies can be found by solving

$$\det \left[H - E_j S \right] = 0 \tag{5.7}$$

5.1.1 Monolayer graphene

Let us apply the introduced procedure to monolayer graphene. Graphene has two atoms per unit cell and one $2p_z$ orbital per atom is taken into account. Graphene has two sets of lattice vectors, $\mathbf{a_1}$, $\mathbf{a_2}$ and $\mathbf{b_1}$, $\mathbf{b_2}$, depending on which the lattice site (see figure XY). The sublattices are labelled A and B. The atomic orbitals are therefore also labelled with a sublattice index, ϕ_A and ϕ_B. The transfer matrix H is

$$H = \begin{pmatrix} \phi_A^* \mathcal{H} \phi_A & \phi_A^* \mathcal{H} \phi_B \\ \phi_B^* \mathcal{H} \phi_A & \phi_B^* \mathcal{H} \phi_B \end{pmatrix} \tag{5.8}$$

$$\equiv \begin{pmatrix} H_{AA} & H_{AB} \\ H_{BA} & H_{BB} \end{pmatrix} \tag{5.9}$$

For the diagonal elements, H_{AA} and H_{BB}, the strongest contribution comes from the interaction of the orbital with itself. The hopping from one A site to another A site is significantly smaller and is therefore neglected. (Makes sense, since the nearest neighbours of an A site are B sites).

$$H_{AA} \approx \frac{1}{N} \sum_{i=1}^{N} \langle \phi_A(\mathbf{r} - \mathbf{R}_{A,i}) | \mathcal{H} | \phi_A(\mathbf{r} - \mathbf{R}_{A,i}) \rangle \equiv \epsilon_A \tag{5.10}$$

$H_{BB} = \epsilon_B$ holds in the analogous way. Since graphene has two identical sublattices A and B, the on-diagonal energies are equal: $\epsilon_A = \epsilon_B$. Off diagonal elements H_{AB} and H_{BA} describe the possibility of hopping from one sublattice to the other.

$$H_{AB} \approx \frac{1}{N} \sum_{i=1}^{N} \sum_{l=1}^{3} e^{i\mathbf{k}\boldsymbol{\delta}_l} \langle \Phi_A(\mathbf{r} - \mathbf{R}_{A,i}) | \mathcal{H} | \Phi_B(\mathbf{r} - \mathbf{R}_{A,i} - \boldsymbol{\delta}_l) \rangle \tag{5.11}$$

$$\equiv -\gamma_0 f(\mathbf{k}), \tag{5.12}$$

where

$$\gamma_0 = -\langle \Phi_A(\mathbf{r} - \mathbf{R}_{A,i}) | \mathcal{H} | \Phi_B(\mathbf{r} - \mathbf{R}_{A,i} - \boldsymbol{\delta}_l) \rangle \tag{5.13}$$

$$f(\mathbf{k}) = \sum_{l=1}^{3} e^{i\mathbf{k}\boldsymbol{\delta}_l} \tag{5.14}$$

$\boldsymbol{\delta}_l$ gives the distance vectors from one given A atom to another B site. The other off-diagnoal element of H is $H_{BA} = H_{AB}^* = -\gamma_0 f^*(\mathbf{k})$. The overlap matrix elements on the diagonal, S_{AA} and S_{BB} equal to one, since

$$S_{AA} = S_{BB} = \langle \Phi_A(\mathbf{r} - \mathbf{R}_{j,i}) | \Phi_A(\mathbf{r} - \mathbf{R}_{j,i}) \rangle = 1. \tag{5.15}$$

For the off-diagonal elements, similar to eq. (5.12), a coefficient s_0 is introduced.

$$S_{AB} = S_{BA} = s_0 f(\mathbf{k}) \tag{5.16}$$

$$s_0 = \langle \Phi_A(\mathbf{r} - \mathbf{R}_{A,i}) | \Phi_B(\mathbf{r} - \mathbf{R}_{B,l}) \rangle \tag{5.17}$$

Finalizing, the Hamiltonian H and the overlap integral matrix S are

$$H = \begin{pmatrix} \epsilon_1 & -\gamma_0 f\left(\mathbf{k}\right) \\ -\gamma_0 f^*\left(\mathbf{k}\right) & \epsilon_B \end{pmatrix} \tag{5.18}$$

$$S = \begin{pmatrix} 1 & s_0 f\left(\mathbf{k}\right) \\ s_0 f^*\left(\mathbf{k}\right) & 1 \end{pmatrix} \tag{5.19}$$

The energy γ_0 and the coefficient s_0 have been determined experimentally [13]: $\gamma_0 = 3.033\text{eV}$ and $s_0 = 0.129$.

5.1.2 Bilayer graphene

Bilayer graphene consists of two layers of graphene, and each of these layers has two sublattices. A lattice site in bilayer graphene can there be in one of the four sublattices A_1, B_1, A_2 and B_2, where the integer 1, 2 labels the layer. Using the notation of the SWM model, [14], [15], the transfer matrix can be written as

$$H = \begin{pmatrix} \epsilon_{A_1} & -\gamma_0 f\left(\mathbf{k}\right) & \gamma_4 f\left(\mathbf{k}\right) & -\gamma_3 f^*\left(\mathbf{k}\right) \\ -\gamma_0 f^*\left(\mathbf{k}\right) & \epsilon_{B_1} & \gamma_1 & \gamma_4 f\left(\mathbf{k}\right) \\ \gamma_4 f^*\left(\mathbf{k}\right) & \gamma_1 & \epsilon_{A_2} & -\gamma_0 f\left(\mathbf{k}\right) \\ -\gamma_3 f\left(\mathbf{k}\right) & \gamma_4 f^*\left(\mathbf{k}\right) & -\gamma_0 f *\left(\mathbf{k}\right) & \epsilon_{B_2} \end{pmatrix} \tag{5.20}$$

The basis of this matrix is $(|\phi_{A_1}\rangle, |\phi_{B_1}\rangle, |\phi_{A_2}\rangle, |\phi_{B_2}\rangle)$ and therefore describes an AB-stacked bilayer system. If the representation of eq (5.20) had the basis $(|\phi_{B_1}\rangle, |\phi_{A_1}\rangle, |\phi_{A_2}\rangle, |\phi_{B_2}\rangle)$, the matrix would describe an AA-stacked bilayer system. In an AB (AA) stacked system, an A_2 atom would be directly above an atom of the B_1 (A_1) sublattice.

In the most general case, the energies ϵ on the diagonal are not equal. The off-diagonal parameters γ are given by

$$\gamma_0 = -\langle\phi_{A_1}|\mathcal{H}|\phi_{B_1}\rangle = -\langle\phi_{A_2}|\mathcal{H}|\phi_{B_2}\rangle, \tag{5.21}$$

$$\gamma_1 = \langle\phi_{A_2}|\mathcal{H}|\phi_{B_1}\rangle, \tag{5.22}$$

$$\gamma_3 = -\langle\phi_{A_1}|\mathcal{H}|\phi_{B_2}\rangle, \tag{5.23}$$

$$\gamma_4 = \langle\phi_{A_1}|\mathcal{H}|\phi_{A_2}\rangle = \langle\phi_{B_1}|\mathcal{H}|\phi_{B_2}\rangle \tag{5.24}$$

The γ_0 parameter describes nearest neighbour hopping within a layer (in-plane hopping) and does therefore contain the factor $f\left(\mathbf{k}\right)$, which is defined as the distance to the surrounding neighbours in one layer. Interlayer hopping between A_2 and B_1 atoms is included with the parameter γ_1. This hopping is vertical from one layer to the other. The parameters γ_3 and γ_4 also describe interlayer hopping, but this hopping is not vertical (it does not connect lattice sites that are directly in line). It can be though of as a combination of in-plane hopping followed by vertical hopping (see figure). The overlap matrix of bilayer graphene can be introduced with the parameters $s_0 = \langle\Phi_{A_1}|\Phi_{B_1}\rangle = \langle\Phi_{A_2}|\Phi_{B_2}\rangle$ and $s_1 = \langle\Phi_{A_2}|\Phi_{B_1}\rangle$ [16]. The parameters s_3 and s_4 are neglected, because they are small (why?).

$$S = \begin{pmatrix} 1 & s_0 f\left(\mathbf{k}\right) & 0 & 0 \\ s_0 f^*\left(\mathbf{k}\right) & 1 & s_1 & 0 \\ 0 & s_1 & 1 & s_0 f\left(\mathbf{k}\right) \\ 0 & 0 & s_0 f^*\left(\mathbf{k}\right) & 1 \end{pmatrix} \tag{5.25}$$

The overlap matrix S is often approximated as a unit matrix and the parameters s_0 and s_1 are neglected. These parameters s_0 and s_1 describe the non-orthogonality of orbitals, which is small for energies $E \leq \gamma_1$.

The tight binding parameters can be determined experimentally using Raman scattering [17] or infrared spectroscopy [18]. The values determined in [18] are

$$\gamma_0 = 3.16, \gamma_1 = 0.381, \gamma_3 = 0.38, \gamma_4 = 0.14. \tag{5.26}$$

5.1.3 Model used in kwant

The bilayer system that is used in this thesis is AB-stacked. The Hamiltonian that is used in the `kwant` software is

$$H = -t \sum_{i,j} e^{i\phi_{i,j}} a_{m,i}^\dagger b_{m,i} - \gamma_1 \sum_j a_{1,j}^\dagger b_{2,j} - \sum_{i,m} \left(\mu_i - (-1)^m \delta_i \right) \left(a_{m,i}^\dagger a_{m,i} + b_{m,i}^\dagger b_{m,i} \right). \tag{5.27}$$

$$H = -\gamma_0 \sum_{i,j} e^{i\phi_{i,j}} a_{m,i}^\dagger b_{m,i} - \gamma_3 \sum_j a_{1,j}^\dagger b_{2,j} - \sum_{i,m} \left(\mu_i - (-1)^m \delta_i \right) \left(a_{m,i}^\dagger a_{m,i} + b_{m,i}^\dagger b_{m,i} \right). \tag{5.28}$$

For implementing the system in kwant, the tight binding model hast to be defined. Means, lattice with corresponding symmetry has to be build and the hoppings between the lattice points have to be definded. First adaption: magnetic field has to be included. It enters in form of a phase (Peierls substitution):

$$\phi_{i,j} = \frac{e}{\hbar} \int_i^j \mathbf{A} d\mathbf{r} \tag{5.29}$$

The parameters X and Y are neglected, the Hamiltonian is of the form

$m = 1, 2$ is index of the layer. The operators $a_{m,i}^\dagger$, $a_{m,i}$ create and annihilate an electron of sublattice A on layer m at site i. In the same way, $b_{m,i}^\dagger$, $b_{m,i}$ are the creation and annihilation operators for the sublattice B. The intralayer hopping parameter t is the same as γ_0 from above and γ_1 is the known interlayer (between dimer) hopping parameter. The onsite energies are

$$\epsilon_{A_1} = \epsilon_{B_1} = \mu_i + \delta_i \tag{5.30}$$
$$\epsilon_{A_2} = \epsilon_{B_2} = \mu_i - \delta_i \tag{5.31}$$
$$\tag{5.32}$$

Here, μ and δ are defined as

$$\mu_i = \frac{\varphi_{BG} + u_i \varphi_{SG}}{2} \tag{5.33}$$
$$\delta_i = \frac{\varphi_{BG} - u_i \varphi_{SG}}{\eta} \tag{5.34}$$

u_i is used as a paramter that defines, if the lattice site i is within a gated region ($u_i = 1$) (underneath a topgate) or not ($u_i = 0$).

5.2 Random matrix theory for transport

5.2.1 Basics about the random matrix theory

To describe the transport through a conducting region of interest, which is in between of two ideal leads. Ideal leads means that there is no disorder present, whereas the conductor is a disordered

system. The question that the random matrix theory is answering, is: how can one describe the transport from one lead, through the disordered region to the other lead? Essential for this transport theory is the work of Landauer (cite!), who described ballistic transport through a 1D channel as a transmission problem.

The transport through the conducting region can be written in terms of an incident wave c^{in} and a reflected/transmitted wave c^{out}. The scattering matrix $\mathcal{S}$ relates the amplitudes of these wave functions.

$$c^{\text{out}} = \mathcal{S} c^{\text{in}}, \tag{5.35}$$

where

$$c^{\text{in}} = \left(a_1^+, a_2^+, \dots a_N^+, b_1^+, b_2^+, \dots b_N^+ \right) \tag{5.36}$$

$$c^{\text{out}} = \left(a_1^-, a_2^-, \dots a_N^-, b_1^-, b_2^-, \dots b_N^- \right) \tag{5.37}$$

The coefficients a represent the left lead and b the right lead. The $\pm$ sign indicates, if it describes a right or left moving electron (see figure). The integer $n = 1, 2, \dots N$ is the index for the propagating modes. In this case, there are N modes in both the left and the right lead. The scattering matrix has the form

$$\mathcal{S} = \begin{pmatrix} r & t' \\ t & r' \end{pmatrix} \tag{5.38}$$

where r, r' are reflection matrices, and t, t' are $N \times N$ transmission matrices. Both the transmission and the reflection matrices have the dimension $N \times N$. The scattering matrix is unitarity, since the current is conserved:

$$\mathcal{S}^{-1} = \mathcal{S}^\dagger. \tag{5.39}$$

Consequently, the matrices $tt^\dagger$, $t't'^\dagger$, $1-rr^\dagger$ and $1-r'r'^\dagger$ have the same set of eigenvalues $T_1, T_2, \dots T_N$, each of them being a real number between 0 and 1.

It is useful to write the scattering matrix $\mathcal{S}$ in terms of the transmission eigenvalues T_n, introducing the matrix $\mathcal{T} = \text{diag}(T_1, T_2, \dots T_n)$. Each of the eigenvalues of $\mathcal{T}$ is a real value between 0 and 1. This rewriting is done in [19] and is called polar decomposition

$$\mathcal{S} = \begin{pmatrix} U & 0 \\ 0 & V \end{pmatrix} \begin{pmatrix} -\sqrt{1-\mathcal{T}} & \sqrt{\mathcal{T}} \\ \sqrt{\mathcal{T}} & \sqrt{1-\mathcal{T}} \end{pmatrix} \begin{pmatrix} U' & 0 \\ 0 & V' \end{pmatrix} \tag{5.40}$$

U, V are are $N \times N$ unitary matrices, I dont know why they are useful.

The scattering matrix relates incoming (c^{in}) states to outgoing (c^{out}) states. It is also possible to look at the transfer matrix M, which relates states from the left lead (c^{left}) to states in the right lead (c^{right}):

$$c^{\text{right}} = M c^{\text{left}} \tag{5.41}$$

where

$$c^{\text{left}} = \left(a_1^+, a_2^+, \dots, a_N^+, a_2^-, a_2^-, \dots a_N^- \right) \tag{5.42}$$

$$c^{\text{right}} = \left(b_1^+, b_2^+, \dots, b_N^+, b_2^-, b_2^-, \dots b_N^- \right) \tag{5.43}$$

$$M = \begin{pmatrix} V & 0 \\ 0 & V'^\dagger \end{pmatrix} \begin{pmatrix} \sqrt{\mathcal{T}^{-1}} & \sqrt{\mathcal{T}^{-1}-1} \\ \sqrt{\mathcal{T}^{-1}-1} & \sqrt{\mathcal{T}^{-1}} \end{pmatrix} \begin{pmatrix} U' & 0 \\ 0 & U\dagger \end{pmatrix} \tag{5.44}$$

Both the transfer matrix M and the scattering matrix S describe the conductive region. The nice feature of the transfer matrix can be seen, if multiple disordered regions, each separated by

ideal leads, are considered. The transfer matrix of the whole system is a multiplication of each regions individual transfer matrix. (which is an advantage, the scattering matrix stuff is then a bit of a fuck off...) The conductance of such a disordered region is given by the sum of the transmission eigenvalues T_n:

$$G = G_0 \sum_{n=1}^{N} T_n, \quad G_0 = \frac{2e^2}{h} \tag{5.45}$$

This is cool. But there is not much context...

5.2.2 Supercurrent of a SNS junction in the scattering matrix approach

Considering an SNS junction. The wave funtions for an incident wave and an reflected/transmitted wave contain now coefficients for electrons and holes:

$$c_N^{\text{in}} = \left(c_e^+(N_1), c_e^-(N_2), c_h^-(N_1), c_h^+(N_2) \right) \tag{5.46}$$

$$c_N^{\text{out}} = \left(c_e^-(N_1), c_e^+(N_2), c_h^-(N_1), c_h^+(N_2) \right) \tag{5.47}$$

N_1 is the number of modes in the left lead, N_2 is the number of modes in the right lead. In the special case of scattering between a normal conductive region and a superconductor, two types of scattering have to be distinguished. For one, there is the normal scattering of electrons and there is Andreev reflection of electrons at the superconductor. The scattering process at the normal region is described by the normal scattering matrix s_N, that connects an incident wave with a reflected/transmitted one.

$$c_N^{\text{out}} = s_N(\epsilon) c_N^{\text{in}} \tag{5.48}$$

This scattering matrix s_N is

$$s_N(\epsilon) = \begin{pmatrix} s_0(\epsilon) & 0 \\ 0 & s_0(\epsilon) \end{pmatrix}, \tag{5.49}$$

where

$$s_0 = \begin{pmatrix} r_{11} & t_{12} \\ t_{21} & r_{22} \end{pmatrix} \tag{5.50}$$

The Andreev reflection process is described by another scattering matrix, the Andreev scattering matrix s_A. For energies $\epsilon < \Delta$, there are no propagating modes inside the superconductor. And for $\Delta_0 \ll E_F$, the normal reflection at the NS interface can be ignored and only Andreev scattering is taken into account.

$$s_A = \alpha(\epsilon) \begin{pmatrix} 0 & r_A \\ r_A^* & 0 \end{pmatrix}, \tag{5.51}$$

with $\alpha(\epsilon) = \exp\left(-i \arccos \frac{\epsilon}{\Delta} \right)$

$$r_A = \begin{pmatrix} e^{i\phi/2} \mathbb{1} & 0 \\ 0 & e^{-i\phi/2} \mathbb{1} \end{pmatrix} \tag{5.52}$$

From the structure of the Andreev scattering matrix, it can be seen that an electron mode is transformed into a hole mode, while the mode index n does not change. This transformation is accompanied by a phase shit of $-\arccos \frac{\epsilon}{\Delta}$, which comes form the decay into the superconducting region. Also, a phase of $\phi/2$ $(-\phi/2)$, where ϕ is the superconducting phase difference, is added for reflection from electron to hole (hole to electron).

A bound state in the SNS junction forms, when

$$c_{\text{in}} = s_A(\epsilon) s_N(\epsilon) c_{\text{in}} \tag{5.53}$$

holds. In the short junction limit, $L \ll \xi$, it holds that

$$s_0(\epsilon) \approx s_0(-\epsilon) \approx s_0(0) \equiv s_0 \tag{5.54}$$

This can be used to simplify the normal scattering matrix $s_N(\epsilon)$ equation (5.49). Using this approximation, the bond state condition eq. (5.53) becomes

$$\begin{pmatrix} s_0^\dagger & 0 \\ 0 & s_0^T \end{pmatrix} \begin{pmatrix} 0 & r_A^* \\ r_A & 0 \end{pmatrix} c_{\text{in}} = \exp\left(i \arccos \frac{\epsilon}{\Delta}\right) c_{\text{in}} \tag{5.55}$$

This can be simplified further. By appliying a Joukowsky (magic) transformation, that i do not understand yet, it is possible to write

$$\begin{pmatrix} 0 & -iA \\ iA & 0 \end{pmatrix} c_{\text{in}} = \frac{\epsilon}{\Delta} \tag{5.56}$$

with $A = \frac{1}{2}(r_A s_0 - s_0^T r_A)$. This leads to

$$A^\dagger A c_{\text{in}} = \frac{\epsilon^2}{\Delta^2} c_{\text{in}} \tag{5.57}$$

So far, the condition for an Andreev bound state has been simplified according to the short junction approach. To get an expression for the current, the free energy F is needed [20]:

$$I = \frac{2e}{\hbar} \frac{dF}{d\phi} \tag{5.58}$$

the free energy F has been calculated as [10]

$$F = -2k_B T \sum_{\epsilon > 0} \ln\left[2 \cosh \frac{\epsilon}{2k_B T}\right] + \dots \tag{5.59}$$

which is the free energy of a non interacting electron . So the current is
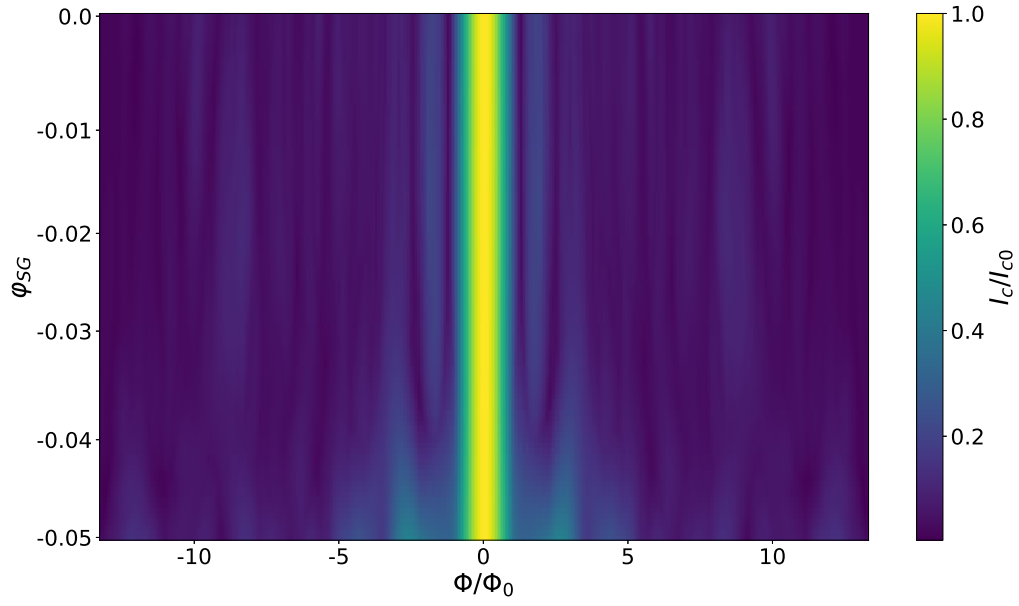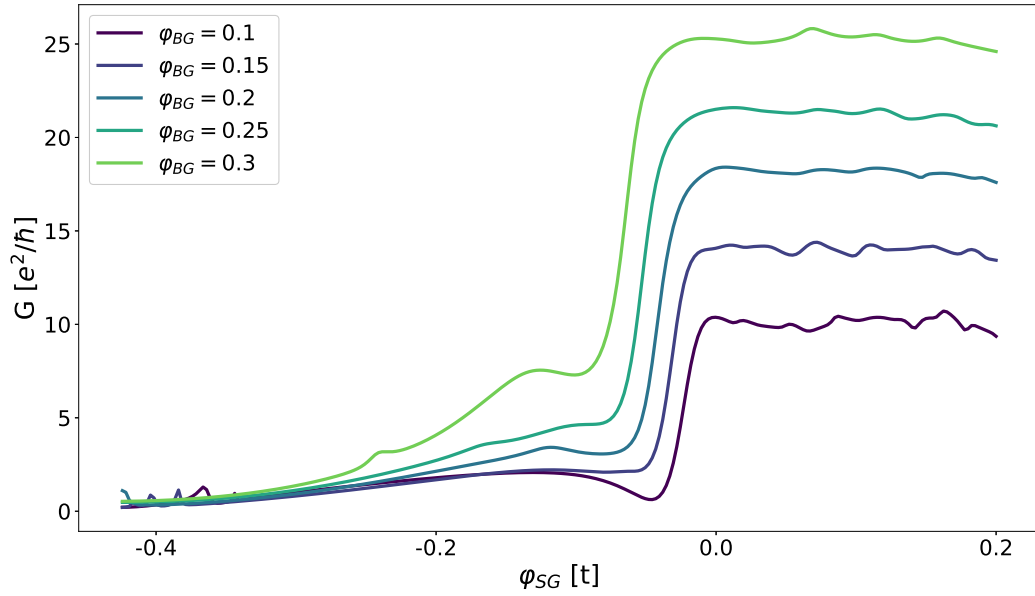
$$I = -\frac{2e}{\hbar} \sum_p \tanh\left(\frac{\epsilon_p}{2k_B T}\right) \frac{d\epsilon_p}{d\phi} \tag{5.60}$$

The derivation of the energy with respect to the phase can be obtained from eq. (5.57).

$$\frac{d\epsilon}{d\phi} = \frac{\Delta^2}{2\epsilon} \frac{\langle c_{\text{in}} | \frac{d(A^\dagger A)}{d\phi} | c_{\text{in}} \rangle}{\langle c_{\text{in}} | c_{\text{in}} \rangle} \tag{5.61}$$

6 Numerical Results

Figure 6.1: *heatmap test*

Figure 6.2: *heatmap test*

7 Conclusion and Outlook

Bibliography

[1] B.D. Josephson. Possible new effects in superconductive tunnelling. *Physics Letters*, 1(7): 251–253, jul 1962.

[2] K. K. Likharev. Superconducting weak links. *Reviews of Modern Physics*, 51(1):101–159, jan 1979.

[3] M. I. Katsnelson, K. S. Novoselov and A. K. Geim. Chiral tunnelling and the Klein paradox in graphene. *Nature Physics*, 2(9):620–625, sep 2006.

[4] Edward McCann. Asymmetry gap in the electronic band structure of bilayer graphene. *Physical Review B*, 74(16):161403, oct 2006.

[5] A. V. Shytov, M. S. Rudner and L. S. Levitov. Klein Backscattering and Fabry-Perot Interference in Graphene Heterojunctions. aug 2008.

[6] F. Chiodi et al. Geometry-related magnetic interference patterns in long SNS Josephson junctions. jan 2012.

[7] Alexandre M. Zagoskin. The half-periodic Josephson effect in an s-wave superconductor-normal-metal-d-wave superconductor junction. *Journal of Physics Condensed Matter*, 9(31), 1997.

[8] Victor Barzykin and Alexandre M. Zagoskin. Coherent transport and nonlocality in mesoscopic SNS junctions: Anomalous magnetic interference patterns. *Superlattices and Microstructures*, 25(5):797–807, 1999.

[9] Hendrik Meier, Vladimir I. Fal'Ko and Leonid I. Glazman. Edge effects in the magnetic interference pattern of a ballistic SNS junction. *Physical Review B*, 93(18):1–13, 2016.

[10] C. W J Beenakker and H. Van Houten. Josephson current through a superconducting quantum point contact shorter than the coherence length. *Physical Review Letters*, 66(23):3056–3059, 1991.

[11] Edward McCann and Mikito Koshino. The electronic properties of bilayer graphene. may 2012.

[12] A. H. Castro Neto et al. The electronic properties of graphene. *Reviews of Modern Physics*, 81(1):109–162, jan 2009.

[13] M.S. Dresselhaus, G. Dresselhaus and R. Saito. Physics of carbon nanotubes. *Carbon*, 33(7): 883–891, jan 1995.

[14] J. W. McClure. Band Structure of Graphite and de Haas-van Alphen Effect. *Physical Review*, 108(3):612–618, nov 1957.

[15] J. W. McClure. Theory of Diamagnetism of Graphite. *Physical Review*, 119(2):606–613, jul 1960.

[16] M Mucha-Kruczynski, E McCann and Vladimir I Fal'ko. Electron hole asymmetry and energy gaps in bilayer graphene. *Semiconductor Science and Technology*, 25(3):033001, mar 2010.

[17] L. M. Malard et al. Probing the Electronic Structure of Bilayer Graphene by Raman Scattering. aug 2007.

[18] A. B. Kuzmenko et al. Determination of the gate-tunable band gap and tight-binding parameters in bilayer graphene using infrared spectroscopy. *Physical Review B*, 80(16):165406, oct 2009.

[19] Pier A. Mello, Pedro Pereyra and Narendra Kumar. A soluble random-matrix model for relaxation in quantum systems. *Journal of Statistical Physics*, 51(1-2):77–94, apr 1988.

[20] C. W. J. Beenakker. Three Universal Mesoscopic Josephson Effects. 1992.